Integrating Effects of Source-Dependent Factors on Sediment-Depth Scaling of Additional Site Amplification to Ground-Motion Prediction Equation

Hongwei Wang[1,2], Chunguo Li[1,2], Ruizhi Wen[*1,2], and Yefei Ren[1,2]

ABSTRACT

It is crucial to include additional site amplification effects resulting from the thick sediment on ground motions in the reliable assessment for seismic hazard in sedimentary basins. Ground-motion residual analysis with respect to ground-motion prediction equation is performed to evaluate additional site amplifications at over 200 K-NET stations within and around Kanto basin. We first investigate the potential effects on additional site amplifications resulted from the sediment depth and several source-dependent factors. Results reveal that source-to-site distance, focal depth, and source azimuth all have nonnegligible effects on additional site amplifications, especially the focal depth. Thick sedimentary sites amplify long-period ground motions from distant earthquakes more strongly than those from local earthquakes. Ground motions from shallow crustal earthquakes generally experience much stronger amplifications than those from those deep subduction earthquakes, much more predominant for long-period ground motions (>1.0 s) at thick sedimentary sites. Meanwhile, we develop the empirical model after integrating contributions from sediment depth, source-to-site distance, and focal depth for predicting additional site amplification effects. Considering the typical case of the distant shallow crustal earthquakes, additional site amplifications at thick sedimentary sites within Kanto basin generally show an increasing trend with the oscillation period increased, whereas they are generally characterized by a decreasing trend at shallow sedimentary sites outside the basin. The mean additional site amplification is up to about 2.0 within Kanto basin, whereas 0.5–0.65 outside Kanto basin, for ground motions at oscillation periods of 2.0–5.0 s. Mean amplifications within Kanto basin are about 3.5 times larger than those outside the basin for long-period ground motions at 2.0–5.0 s. Sites northeast to Kanto basin show the largest amplifications up to about 3.0 at periods of 0.15 and 5.0 s, which may be resulted from the basin edge effects.

KEY POINTS

- Distance, focal depth, and source azimuth affect sediment-depth scaling of additional site amplification.
- Thick sedimentary sites cause stronger amplifications to ground motions in distant shallow crustal earthquakes.
- Amplification model in Kanto basin considering sediment depth and source-dependent factors is first proposed.

Supplemental Material

INTRODUCTION

The near-surface geological condition plays a critical role in significantly modifying and amplifying seismic ground motion (Borcherdt, 1970). It has been principally interpreted by the trapping effects on seismic waves due to the impedance contrast between the horizontal sedimentary layers and the underlying bedrock (Cornou and Bard, 2003). Consequently, the site amplification effects were generally evaluated by the 1D transfer

1. Institute of Engineering Mechanics, China Earthquake Administration, Harbin, China, https://orcid.org/0000-0001-9706-6230 (HW); https://orcid.org/0000-0003-2066-1888 (CL); https://orcid.org/0000-0001-6381-9425 (RW); https://orcid.org/0000-0003-1097-8259 (YR); 2. Key Laboratory of Earthquake Engineering and Engineering Vibration of China Earthquake Administration, Harbin, China

*Corresponding author: ruizhi@iem.ac.cn

Cite this article as Wang, H., C. Li, R. Wen, and Y. Ren (2021). Integrating Effects of Source-Dependent Factors on Sediment-Depth Scaling of Additional Site Amplification to Ground-Motion Prediction Equation, *Bull. Seismol. Soc. Am.* **112**, 400–418, doi: 10.1785/0120210134

© Seismological Society of America

Downloaded from http://pubs.geoscienceworld.org/ssa/bssa/article-pdf/112/1/400/5519095/bssa-2021134.1.pdf
by Yefei Ren

function in the frequency domain theoretically calculated using the shallow soil shear- (S-) wave velocity profiles.

However, the large-amplitude surface waves can be generated on the heterogeneous interface of 2D and 3D geological structures (e.g., the sedimentary valley and basin), and are subsequently trapped within these structures. The surface waves, always arriving later than the direct body waves and characterized by the long-period shaking, can greatly amplify the ground-motion amplitude and prolong the duration of strong shaking. Such phenomenon is commonly known as basin effects, which have been delineated in some theoretical studies (e.g., Bard and Bouchon, 1980; Kawase and Aki, 1989). It is likely that severe ground shaking is localized at the basin edges due to the strong constructive interference of the direct body waves with the basin-generated surface waves, which has been verified to be the main cause of the enhanced earthquake damage, for example, the Kobe damage belt occurred in the 1995 Kobe earthquake (Kawase, 1996), and the particular damage in Santa Monica area in the 1994 Northridge earthquake (Graves *et al.*, 1998). Basin effects are generally one of the predominant reasons for the additional site amplifications with respect to the 1D site amplification effects.

The basin-generated surface waves have been widely identified from the seismic waveforms over many sedimentary basins worldwide with various geological structures and sedimentary thickness, for example, a large number of small-size intramountain basins in Central and Northern Italy (e.g., Rovelli *et al.*, 2001; Pacor *et al.*, 2007; Luzi, *et al.*, 2019), the Grenoble basin in French Alps (e.g., Cornou *et al.*, 2003), the western Taiwan coastal plain (e.g., Wang *et al.*, 2006), the Kanto basin in Japan (e.g., Koketsu and Kikuchi, 2000; Miyake and Koketsu, 2005; Furumura and Hayakawa, 2007), the Po Plain basin in North Italy (e.g., Abraham *et al.*, 2015), the Seattle and Tacoma basins in Washington State (e.g., Thompson *et al.*, 2020), the Ashigara valley in Japan (e.g., Kawase and Sato, 1992), and so forth. Meanwhile, the 3D seismic-wave propagation numerical simulations also clearly illustrated the generation of surface waves at the basin edge and their propagation through the superficial sediment (e.g., Sato *et al.*, 1999; Furumura and Hayakawa, 2007; Roten *et al.*, 2008; Hartzell *et al.*, 2016). For the first time, Sato *et al.* (1999) performed the 3D finite-difference simulation to successfully reproduce the basin-generated surface waves in Kanto basin during a moderate earthquake and the Great 1923 Kanto earthquake.

Reliable evaluation of the additional site amplification effects related to basin effects is crucial for accurate predictions of the ground-motion intensity in the basin. Considering the complex 3D geological structure, the 1D transfer function derived from the *S*-wave velocity profile cannot completely capture the additional site amplification effects on long-period ground motions, even the 2D numerical approach (Olsen, 2000; Smerzini *et al.*, 2011). As a result, the 3D numerical simulation has been widely utilized to assess the basin effects on amplifying ground motions (e.g., Semblat *et al.*, 2002; Volk *et al.*, 2017; Wirth *et al.*, 2019; Mouzakiotis *et al.*, 2020; Thompson *et al.*, 2020). At the same time, the basin effects were directly analyzed using the observed ground-motion recordings. The site-to-bedrock spectral ratio of the whole ground-motion waveform was verified to be an effective approach to estimate the basin effects (Cornou *et al.*, 2003; Roten *et al.*, 2008; Hartzell *et al.*, 2016; Luzi *et al.*, 2019). However, it is usually hard to find an appropriate bedrock reference site. In many studies, ground-motion residuals with respect to the ground-motion prediction equation (GMPE) were calculated to estimate the additional site amplifications associated to basin effects and further develop the empirical models (Choi *et al.*, 2005; Skarlatoudis *et al.*, 2015; Marafi *et al.*, 2017; Moschetti *et al.*, 2020). In recent years, surface-wave propagation effects in sedimentary basin were also exploited from the ambient seismic field, for example, in the Los Angeles basin (Denolle, Dunham, *et al.*, 2014) and the Kanto basin (Denolle, Miyake, *et al.*, 2014).

Current studies have commonly modeled the additional site amplification associated to basin effects as a function of sediment depth, for example, Z_1, depth to *S*-wave velocity (V_S) equal to 1.0 km/s (e.g., Boore *et al.*, 2014); $Z_{2.5}$, depth to $V_S =$ 2.5 km/s (e.g., Marafi *et al.*, 2017); $Z_{1.4}$, depth to $V_S = 1.4$ km/s (e.g., Morikawa and Fujiwara, 2013; Dhakal *et al.*, 2015), and suggested the application in seismic hazard assessments. However, some studies have furnished enough evidence on the significant dependency of basin effects on source-to-site distance, source azimuth, focal depth, and earthquake type according to ground-motion recordings, ambient seismic measurements, and earthquake numerical simulations (e.g., Denolle, Miyake, *et al.*, 2014; Wirth *et al.*, 2019; Lai *et al.*, 2020; Moschetti *et al.*, 2020; Thompson *et al.*, 2020). Accordingly, more complicated models integrating multiple factors appear essential for the accurate predictions of basin amplifications to ground motion.

The Kanto basin and the surrounding areas are characterized by the active and complex seismicity principally due to the nearby triple junction associated with the Eurasian, Pacific, and Philippine Sea plates (e.g., Stein *et al.*, 2006; Wu *et al.*, 2007; Ishise *et al.*, 2015; Hashima *et al.*, 2016). The Philippine Sea plate and the underlying Pacific plate are all wedged beneath the Kanto basin. It has been subjected to numerous shallow crustal and deep subduction earthquakes. The basin-generated surface-wave field in Kanto basin has been generally observed in ground-motion recordings during some earthquakes, for example, the 1998 M 5.7 off the Izu peninsula earthquake (Koketsu and Kikuchi, 2000), the 2004 M_{JMA} 7.4 off the Kii peninsula earthquake (Miyake and Koketsu, 2005), the 2004 M_{w} 6.6 Chuetsu earthquake (Furumura and Hayakawa, 2007), and the 2011 M_{w} 9.0 Tohoku earthquake and its aftershocks (Tsuno *et al.*, 2012), as well as in the

Downloaded from http://pubs.geoscienceworld.org/ssa/bssa/article-pdf/112/1/400/5519095/bssa-2021134.1.pdf
by Yefei Ren

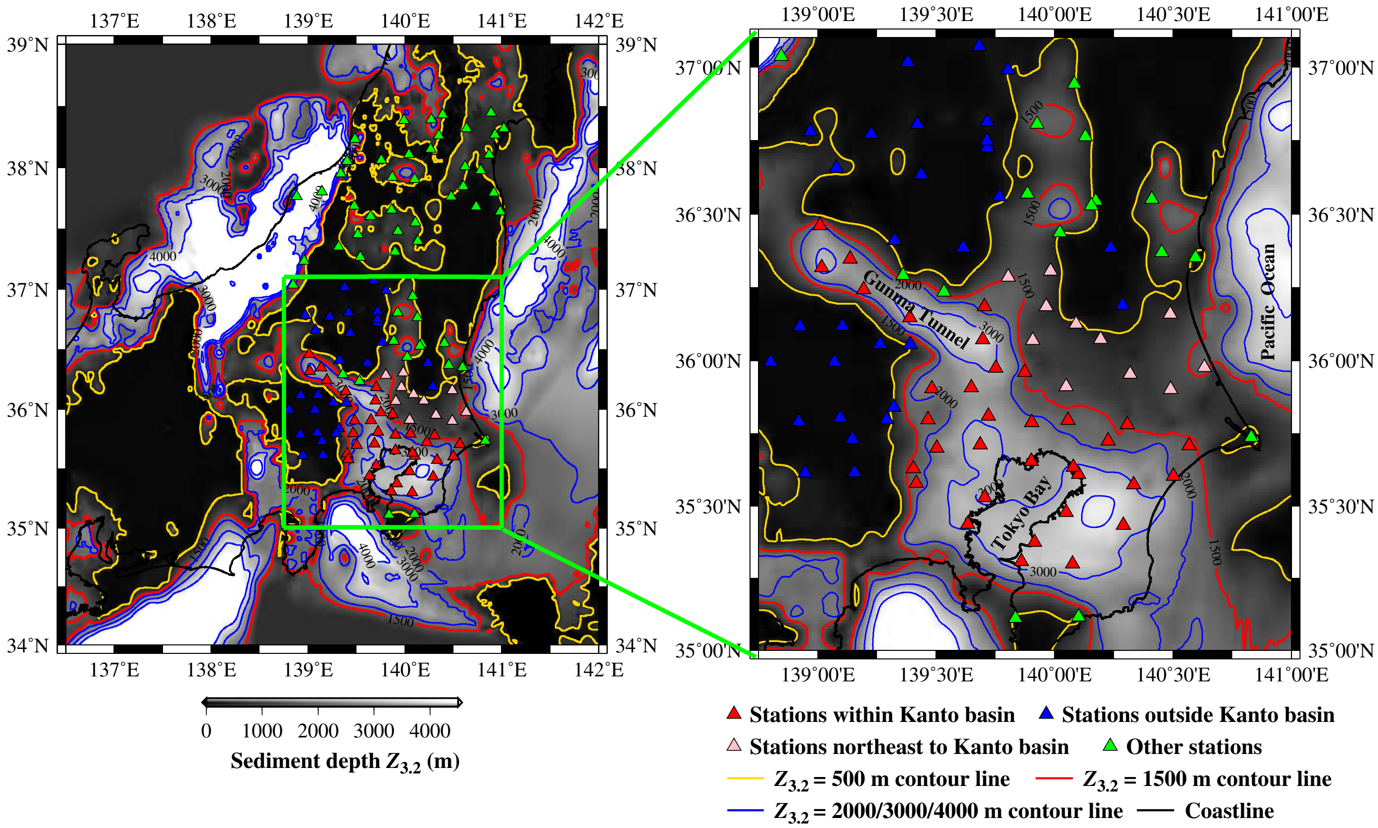

Figure 1. $Z_{3.2}$ contour maps of the Kanto basin and the surrounding areas. Triangles represent the 127 K-NET stations where the additional site amplifications are derived from distant shallow crustal earthquakes. Gold, red, and blue lines indicate the contour lines of $Z_{3.2}$ equal to 500 m, 1500 m, and 2000–4000 m at a constant interval of 1000 m, respectively. Black solid line indicates the coastline. Green rectangle indicates the location of Kanto basin. The color version of this figure is available only in the electronic edition.

ambient seismic field measurements (Denolle, Miyake, *et al.*, 2014; Boué *et al.*, 2016). Dense ground-motion observation network in and around Kanto basin has accumulated abundant ground-motion data, fundamental for additional site amplification estimations related to basin effects using the residuals from a GMPE. In this study, residuals of ground motions during earthquakes in and around Kanto basin with respect to the GMPE in Japan are calculated and decomposed to estimate the additional site amplifications. We further discuss the potential effects of multiple factors on the amplifications, including the sediment depth, source-to-site distance, magnitude, focal depth, and source azimuth. Furthermore, an empirical model for predicting additional site amplification related to basin effects is developed by accounting for multiple factors. Finally, we emphasize the prominent differences of additional site amplifications at sites within and outside Kanto basin.

GEOLOGICAL SETTING

The Kanto basin, a large-scale sedimentary basin, is surrounded by mountains on the west and north where the stiffer bedrocks are exposed, and by the Pacific Ocean on the east and south. The sediments filling the Kanto basin can be divided into three groups from surface to basement according to geological surveys and borehole measurements, that is: the Shimosa group with $V_S = 0.4$–0.6 km/s, the Kazusa group with $V_S = 1.0$ km/s, and the Miura group with $V_S = 1.7$ km/s (Koketsu *et al.*, 2009). The basement velocity gradually increases from south to north due to the younger bedrock toward the south (Koketsu *et al.*, 2009). The Kanto basin reaches a maximum depth up to 4.0 km to the east side of the Tokyo bay according to the Japan Integrated Velocity Structure Model of the Headquarters for Earthquake Research Promotion (HERP) (see Data and Resources), when the $V_S = 3.2$ km/s isosurface is used as a proxy of the sediment depth (Fig. 1). The boundary of the Kanto basin is approximately illustrated by the contour line of $Z_{3.2}$ (depth to $V_S = 3.2$ km/s) equal to 1.5 km in this study, as shown in Figure 1. The thickness of the sediments is larger than 2.0 km from the center (Tokyo bay) to the northwest (Gunma tunnel). The basin is opened to the southeast, whereas a sharp basin edge can be clearly observed at the west. In the present study, the HERP velocity model is used for the depth of $Z_{3.2}$ in the correction equations explained later. The HERP velocity model is easily available and was found to have satisfactory results for the simulation of long-period ground motions in the Kanto basin (e.g., Dhakal and Yamanaka, 2013).

Downloaded from http://pubs.geoscienceworld.org/ssa/bssa/article-pdf/112/1/400/5519095/bssa-2021134.1.pdf
by Yefei Ren

GROUND-MOTION DATA

We downloaded 39,207 ground-motion acceleration time histories recorded by K-NET stations during 301 earthquakes with $M_{JMA} = 5.0$–8.0 that occurred in and around Kanto basin (latitude 34°–38° N, longitude 137°–142° E) from January 2010 to December 2019 (see Data and Resources).

The high-resolution focal locations for these earthquakes are retrieved from the Japan Meteorological Agency (JMA) Uniformed Hypocenter Catalog (see Data and Resources). The focal mechanisms for 256 earthquakes are obtained from the Global Centroid Moment Tensor Project (see Data and Resources), and their fault types are specified by the plunge of the P and T axes (Boore *et al.*, 2013). We further obtain the focal mechanisms for additional 28 earthquakes from the Focal Mechanism Catalog of the High Sensitivity Seismograph Network Japan (see Data and Resources) and specify their fault types according to the rake angle (Ancheta *et al.*, 2013). These 284 in total 301 earthquakes with available focal mechanisms are classified into 96 normal events, 147 reverse events, 27 strike-slip events, and 14 oblique ones. Their moment magnitudes are in the range of 4.5–6.9. We also classify these 284 events into different tectonic categories, including 80 shallow crustal events, 42 subduction interface events, 102 slab events, and 60 upper mantle events, using the classification schemes proposed by Zhao *et al.* (2015) and the subduction zone geometries defined by the Slab1.0 model (Hayes *et al.*, 2012).

We first eliminate the near-field recordings with source-to-site distances smaller than 10 km to avoid the unreliable distance estimation and the occurrence of strong nonlinear soil behavior as much as possible. Then, the magnitude-dependent distance limits, which are intuitively expressed by a straight line from 120 km for M_w 4.5 to 300 km for M_w 6.9 in the distance–magnitude plots, are applied to the ground-motion dataset to avoid the bias as much as possible due to the triggered threshold (Abrahamson *et al.*, 2016; Zhao *et al.*, 2016). In this study, the rupture distances for recordings from 24 earthquakes with $M_w \geq 6.0$ and the hypocentral distances for recordings from other events are regarded as the source-to-site distance metrics, respectively. The rupture distance is estimated according to the following steps: (1) The area of the fault plane is constrained by its empirical relationship with the M_w and the tectonic category (Murotani *et al.*, 2008, 2015; Irikura and Miyake, 2011; Iwata and Asano, 2011), the geometry of the fault plane (length and width of the fault plane, along the strike and dip, respectively) is then empirically defined by an aspect ratio of 1.7. (2) The probability density functions provided by Mai *et al.* (2005) are used to define the occurrence probability of the hypocenter position on the fault plane. The down-dip hypocenter position can be modeled by a Weibull distribution for strike-slip and crustal dip-slip earthquakes and a narrow Gamma distribution for subduction dip-slip earthquakes. The along-strike hypocenter position can be modeled by a normal distribution. With the geographical coordinates of the hypocenter fixed, totally 121 hypocenter positions on fault plane are considered in this study. (3) The rupture distances for a specific site are all calculated according to 121 dummy rupture planes with various hypocenter positions on fault plane, and the weighted average is used as the rupture distance. The weights are equal to the occurrence probabilities for various hypocenter positions. Recordings at stations with unavailable borehole velocity profile or with available velocity profile but profile depth smaller than 10 m are also eliminated due to the unknown or unreliable V_{S30} values (V_{S30}, time-weighted average shear-wave velocity over the upper 30 m). The extrapolation relation proposed by Wang and Wang (2015) for Japan sites is used to estimate V_{S30} values for those K-NET stations with profile depth greater than 10 km but smaller than 30 m.

We finally assemble 15,218 ground-motion recordings at 422 K-NET stations from 211 M_w 4.5–6.9 earthquakes in our dataset, as shown in Figure 2a. Figure 2b,c shows the focal depth–magnitude and the distance–magnitude plots for our dataset, respectively. These recordings are first processed for calculating the 5%-damped pseudospectral acceleration (PSA). The cosine tapers with a width of 2.0 s are used near the beginning and end of the waveforms to avoid truncation effects. Then, the zero pads with a sufficient length are appended to the beginning and end (Boore, 2005). The Butterworth band-pass acausal filter is performed in the frequency domain with the high-pass and low-pass corner frequencies equal to 0.16 and 30.0 Hz, respectively. The horizontal PSA is represented by the geometric mean of PSAs at both horizontal components of the ground motion. Figure 3 shows the horizontal PSAs at oscillation periods of 0.3 and 3.0 s, respectively. The PSAs are shown in five magnitude bins differentiated by colors. Figure 3 also plots the predicted medians on hard-rock sites in shallow crustal reverse earthquakes with M_w equal to 4.5, 5.5, and 6.5, respectively, using the GMPE developed by Zhao *et al.* (2006; hereafter, Zhao06 model) based on the horizontal PSAs of strong-motion recordings all over Japan.

GROUND-MOTION RESIDUAL ANALYSIS

The residual, denoted ε_{es}, is expressed by the observed horizontal PSA minus the median value predicted by GMPE in natural log units. The residual can be decomposed into interevent residual (δB_e), intraevent residual (δW_{es}), and a mean bias term c, that is,

$$\varepsilon_{es} = \delta B_e + \delta W_{es} + c, \quad (1)$$

in which the subscript e refers to the earthquake, and subscript s refers to the recording at station s in earthquake e. The δB_e represents the average deviation of the observed ground motion from an earthquake e with respect to the mean of the predicted ground motion. The δW_{es} represents the degree of misfit between an individual observation at a station and the earthquake-specific median prediction (e.g., Wen *et al.*, 2018). It is mainly related to path and site effects.

Downloaded from http://pubs.geoscienceworld.org/ssa/bssa/article-pdf/112/1/400/5519095/bssa-2021134.1.pdf
by Yefei Ren

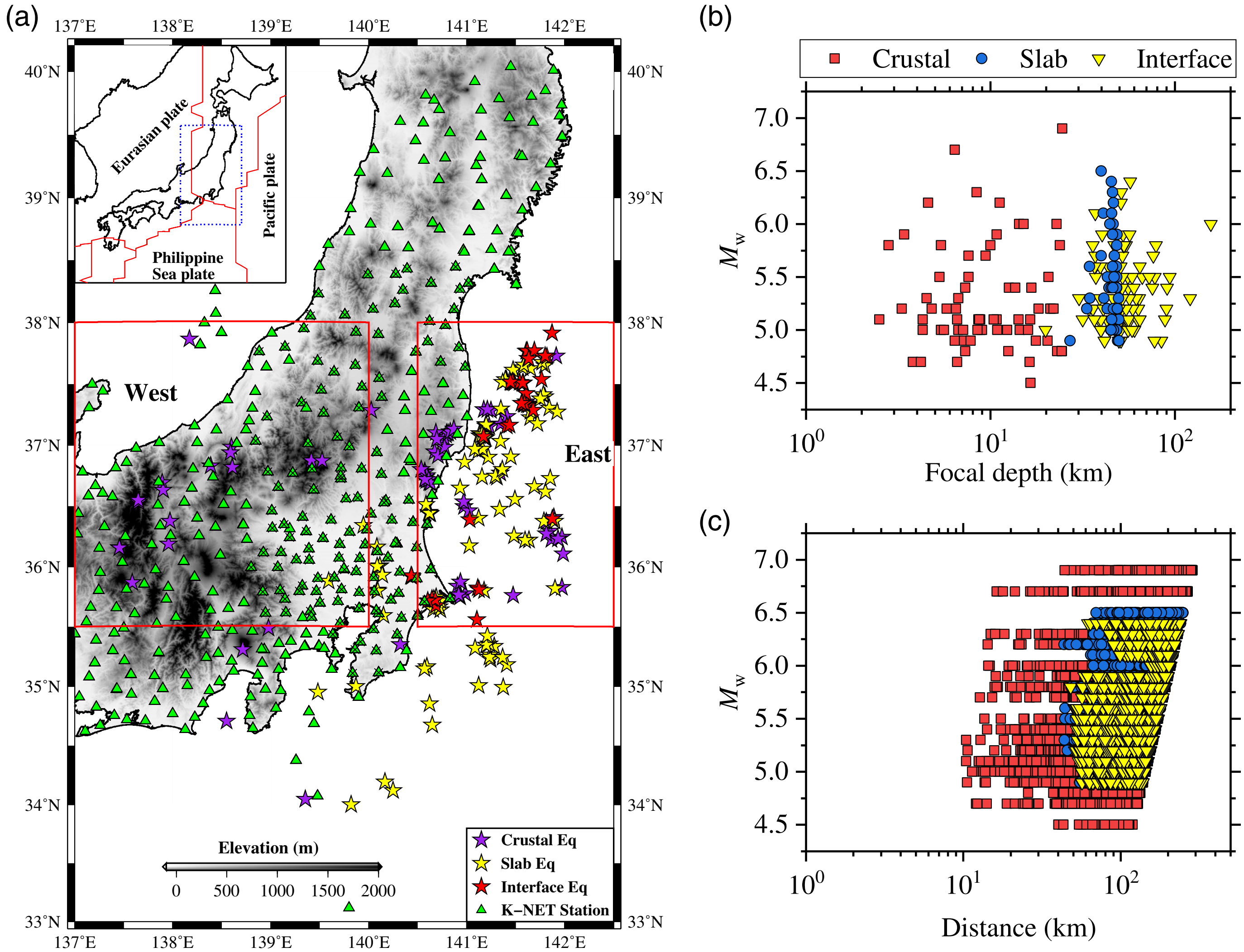

Figure 2. (a) Map of earthquake epicenters (stars) and K-NET stations (triangles) for ground-motion dataset considered in this study. Triangles with crosses indicate 127 K-NET stations where the basin amplifications are derived from shallow crustal distant earthquakes. (Inset) The blue rectangle indicates the location of the study region in Japan, and the red lines indicate the boundary of plates. (b) Moment magnitude versus focal depth and (c) moment magnitude versus source-to-site distance for those earthquakes considered. The color version of this figure is available only in the electronic edition.

In this study, the Zhao06 model is used to provide the predicted medians. The site class term instead of the individual V_{S30}-scaling site term is used in the Zhao06 model to describe the site effects. Five site classes, classified base on the site dominant periods, are considered in this model, approximately corresponding to the hard rock, rock, hard soil, medium soil, and soft soil. Before calculating the predicted medians in this study, the site classes are first classified according to the site dominant periods estimated from the site V_{S30} values. The site class term in the Zhao06 model was directly determined by the regression analysis using the observed PSAs, rather than by the theoretically calculated 1D site amplifications, according to the 1D soil *S*-wave velocity profiles. The site class term in the Zhao06 model may thus combine the 1D site amplification and a part of the other site amplification accounting for the basin or terrain effects. Therefore, the average of the δW_{es} values at station *s* over all events can be approximately defined as the additional site amplification at station *s* with respect to the site class term in the Zhao06 model. For those stations in Kanto basin, the additional site amplification is mainly related to the basin effects.

The linear mixed-effects regression (Abrahamson and Youngs, 1992) is performed to decompose ε_{es}. The δB_e and *c* values are obtained and plotted against oscillation period in Figure 4a,b. The *c* values, close to zero at short periods but generally smaller than zero at long periods, approximately show a decreasing trend with increasing oscillation period. The negative *c* values indicate that the Zhao06 model overpredicts ground motions. The δB_e values at each oscillation period fluctuate around zero and generally show an average of zero. Figure 4c,d shows the δW_{es} values against distance for PSAs at oscillation periods of 0.3 and 3.0 s, respectively. The distance

Downloaded from http://pubs.geoscienceworld.org/ssa/bssa/article-pdf/112/1/400/5519095/bssa-2021134.1.pdf
by Yefei Ren

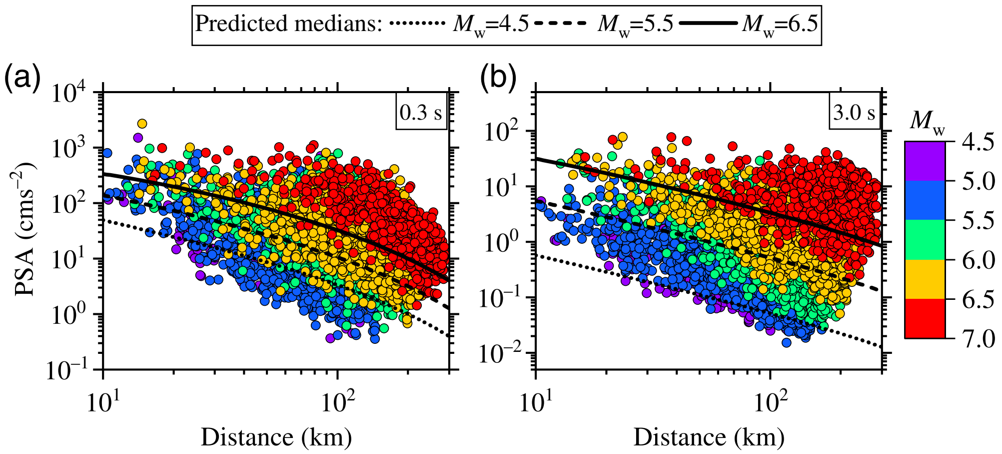

Figure 3. Horizontal 5%-damped pseudospectral accelerations (PSAs) at oscillation periods of (a) 0.3 and (b) 3.0 s for recordings considered in this study. The predicted medians by the Zhao *et al.* (2006; referred as Zhao06 model) on hard-rock sites in shallow crustal reverse earthquakes with M_w equal to 4.5 (dotted line), 5.5 (dashed line), and 6.5 (solid line) were also plotted. The color version of this figure is available only in the electronic edition.

trend in δW_{es} appears to occur at far field, especially for those δW_{es} values at oscillation period of 0.3 s.

The discrepancy in far-field apparent anelastic attenuation between the observed ground motions and the GMPE may greatly affect the additional site amplification estimation. Such discrepancy can be illustrated intuitively from the distance trend in δW_{es} at far field. Following Boore *et al.* (2014), we adopted the path-correction term δW_{esp} to describe the potential distance trend in δW_{es} at far field, and δW_{esp} is expressed as

$$\delta W_{esp} = \Delta c_3 R_{es} + \Delta W_{1R}, \tag{2}$$

in which R_{es} is the distance of station s to earthquake e. ΔW_{IR} is approximately the mean δW_{es} at close distance. Slope Δc_3 is an index for quantifying the discrepancy in far-field anelastic attenuation. $\Delta c_3 = 0$ implies no perceptible distance trends in δW_{es} at far field. Negative (or positive) Δc_3 indicates that δW_{es} values have downward (or upward) distance trend at far field. Values of Δc_3 and ΔW_{IR} are plotted against oscillation period in Figure 4e. The yield Δc_3 values are always less than zero at short oscillation periods ($< \sim 1.0$ s) whereas greater than zero at long oscillation periods ($> \sim 1.0$ s). The negative or positive Δc_3 values verify the discrepant far-field anelastic attenuation.

After correcting the path attenuation, the additional site amplification A_s at station s is expressed as

$$A_s = \exp\left[\sum_{e=1}^{N} (\delta W_{es} - \delta W_{esp})/N\right], \tag{3}$$

in which N is the number of earthquake events recorded by station s. The minimum N no less than 10 is used in this study. The additional site amplification values for 20 oscillation periods from 0.05 to 5.0 s are calculated at 224 K-NET stations according to equation (3).

FACTORS AFFECTING ADDITIONAL SITE AMPLIFICATION

Sediment depth

Sediment depth has been typically recognized as a fundamental factor affecting the basin amplification of earthquake ground motions (e.g., Choi *et al.*, 2005; Marafi *et al.*, 2017). Consistently, the pronounced effects of sediment depth $Z_{3.2}$ are observed in the additional site amplification values at 224 K-NET stations at some oscillation periods, as plotted in Figure 5. It is first noted that the sediment-depth scaling of additional site amplification is dependent on the oscillation period. Additional site amplification values at the shortest period (0.05 s) show a decreasing trend from amplification to deamplification with the increasing $Z_{3.2}$, which can be explained by the reducing body-wave energy due to the increased number of wave cycles with the increasing sediment depth. However, the increasing trends from deamplification to amplification always occur in the amplifications at medium-to-long periods (>0.3 s), which can be explained by the strong amplifications due to the long-period surface waves prone to be produced at sites atop the thick sediment. At long periods (≥1.0 s), additional site amplification values are generally greater than 1.0 at sites atop the thick sediment, whereas lower than 1.0 at those sites with shallow sedimentary thickness. The simple linear relation of additional site amplification value A_s associated with sediment depth $Z_{3.2}$ both in natural log units is adopted to approximately describe the sediment-depth scaling of additional site amplification, that is,

$$\ln(A_s) = c_0 \ln(Z_{3.2}) + c_1. \tag{4}$$

The linear expression has also been adopted by Denolle, Miyake, *et al.* (2014) to account for basin depth scaling. We fit coefficients c_0 and c_1 at all oscillation periods using the linear least-squares regression, as listed in Table 1. Even if the best-fitting regressions (solid lines in Fig. 5) are in good agreement with the general trends, the calculated additional site amplification values scatter significantly, which may be attributed to potential effects of earthquake source, for example, source-to-site distance, focal depth, magnitude, or more.

Downloaded from http://pubs.geoscienceworld.org/ssa/bssa/article-pdf/112/1/400/5519095/bssa-2021134.1.pdf
by Yefei Ren

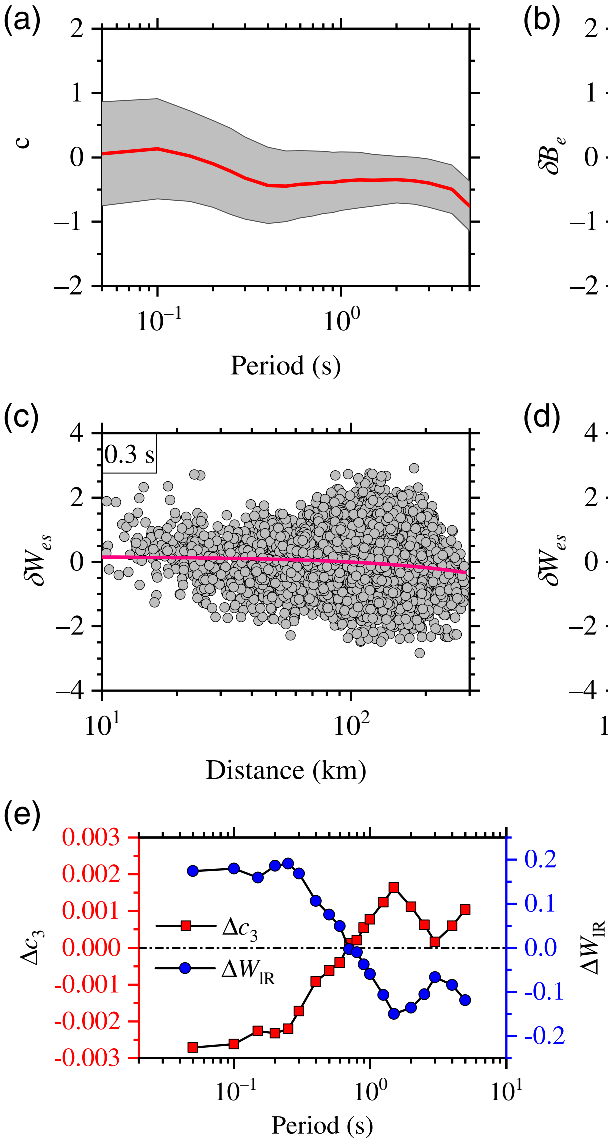

Figure 4. (a) The bias terms c and its 95% confidence intervals. (b) The δB_e values against oscillation period. (c) The δW_{es} values against distance for PSAs at oscillation period of 0.3 s. (d) The δW_{es} values against distance for PSAs at oscillation period of 3.0 s. (e) Values of Δc_3 and ΔW_{IR} in the path-correction term to describe the distance trend in the intraevent residual at far field. The color version of this figure is available only in the electronic edition.

Source-to-site distance

To evaluate whether the source-to-site distance potentially affects the additional site amplification, the whole ground-motion dataset is first divided into two subsets according to source-to-site distances, that is, the local dataset with $R_{es} < 100$ km and the distant dataset with $R_{es} > 100$ km. According to equation (3), we then calculate the additional site amplification values at 94 and 173 K-NET stations using the local and distant datasets, respectively. Because of the reduced number of recordings at station from the subset, the limit on minimum N in equation (3) leads to the fewer stations where additional site amplifications can be calculated. Totally 86 stations are included in the 94 stations and the 173 stations at the same time. Additional site amplifications at these 86 stations derived from both distance-dependent subsets are finally used to calculate deviations to those derived from the whole dataset, as shown in Figure 6. Deviation is denoted by $\ln(A_{dis}/A_s)$, in which A_{dis} represents the additional site amplification derived from the distance-dependent subset.

Distance effects cannot be ignored clearly shown in the deviation plots against $Z_{3.2}$. It is found that sites atop the thick sediment (mainly in Kanto basin) appear to greatly amplify the long-period ground motions from distant earthquakes more than those from local earthquakes. Similar results, larger amplifications associated to earthquakes located farther from the basin, have been observed both in ground-motion recordings and in numerical simulations in some previous studies (e.g., Olsen, 2000; Luzi *et al.*, 2019; Wirth *et al.*, 2019). Wirth *et al.* (2019) explained that basin geometry focuses wave energy, resulting in more amplified ground shaking in the regions of the basin farthest away from the earthquake rupture. They also pointed out that distant earthquake is likely to cause large amplification due to mode conversions and reverberations by the shallowing of sediment thickness near the basin-edge. Moreover, we also note contrary distance effects at sites with shallow sedimentary thickness, which generally results in larger amplifications to the long-period ground motions from local earthquakes than distant ones. A hyperbolic tangent functional form is applied to depict the distance-dependent amplification effects that modify the default sediment-depth scaling, that is,

$$\ln(A_{dis}/A_s) = a_1 \tanh[\ln(Z_{3.2}) - a_2] + a_3, \quad (5)$$

in which a_1, a_2, and a_3 are regression coefficients obtained by nonlinear least-squares regression, listed in Table 1 for local

Downloaded from http://pubs.geoscienceworld.org/ssa/bssa/article-pdf/112/1/400/5519095/bssa-2021134.1.pdf
by Yefei Ren

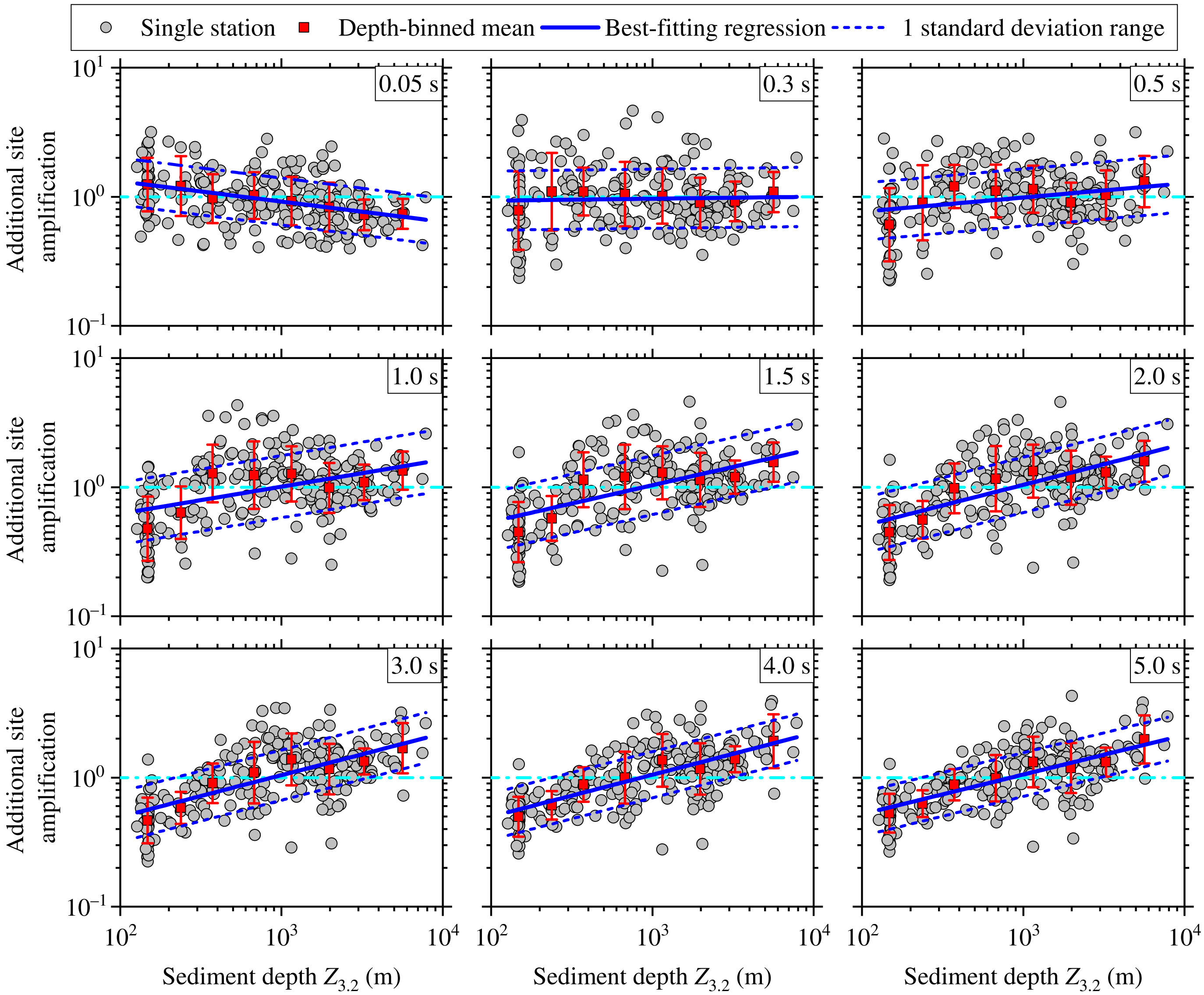

Figure 5. Additional site amplification values for ground motions at oscillation periods from 0.05 to 5.0 s versus sediment depth $Z_{3.2}$. The depth-binned means are represented by squares, with bars indicating standard errors. Solid lines are regressed to describe the additional site amplification as a function of $Z_{3.2}$, and the dashed lines indicate the one standard deviation range. The color version of this figure is available only in the electronic edition.

and distant datasets, respectively. The best-fitting lines well represent the overall variation of distance-dependent deviation with sediment depth, as shown in Figure 6.

Magnitude

Furthermore, two groups (one with $M_w < 5.5$ and the other with $M_w \geq 5.5$) are separated from the local dataset ($R_{es} < 100$ km), and then used to calculate the additional site amplifications at 75 and 34 K-NET stations, respectively, following equation (3). Deviations of additional site amplifications at 34 stations, both from M_w-dependent local dataset to those derived from the local dataset, are plotted in Figure 7. It is found that deviations slightly fluctuate around zero and are independent of the earthquake magnitude, especially at sites atop the thick sediment. Similarly, Skarlatoudis *et al.* (2015), Marafi *et al.* (2017) also found that earthquake magnitude shows negligible effects on basin amplifications, even if small number of earthquakes were considered in their studies.

Focal depth

In this study, focal depths are generally smaller than 30 km for crustal earthquakes and larger than 30 km for subduction earthquakes (Fig. 2b). To analyze the effects of focal depth, both distance-dependent subsets are further divided into four smaller dataset according to the focal depth (Dep), that is, $R_{es} < 100$ km & Dep < 30 km, $R_{es} < 100$ km & Dep > 30 km, $R_{es} > 100$ km & Dep < 30 km, and $R_{es} > 100$ km & Dep > 30 km. Four aforementioned datasets are used to calculate the additional site amplifications at 61, 46, 127, and 74 K-NET stations, respectively, using equation (3). These

Downloaded from http://pubs.geoscienceworld.org/ssa/bssa/article-pdf/112/1/400/5519095/bssa-2021134.1.pdf
by Yefei Ren

TABLE 1
Coefficients of the Additional Site Amplification Model

			$R_{es} < 100$ km			$R_{es} > 100$ km			Dep < 30 km			Dep > 30 km		
T/s	c_0	c_1	a_1	a_2	a_3	a_1	a_2	a_3	b_1	b_2	b_3	b_1	b_2	b_3
0.05	−0.157	0.998	−0.0334	−304.8551	−0.0337	0.0437	−533.1999	0.0444	0.0951	6.6839	0.0778	−0.1479	7.1132	−0.1267
0.1	−0.165	1.045	−0.0222	5.3630	−0.0750	0.0585	−100.4356	0.0586	0.0693	6.6681	0.1473	−0.1308	7.1045	−0.2060
0.15	−0.084	0.506	−0.0487	6.2595	−0.0925	0.0323	5.6019	0.1075	0.0702	6.6518	0.2058	−0.1464	7.1766	−0.2779
0.2	−0.039	0.200	−0.0301	6.4079	−0.1081	0.0697	−157.4165	0.0700	0.0824	6.7763	0.2237	−0.1781	7.3498	−0.3149
0.25	−0.012	0.031	−0.0476	−233.7442	−0.0479	0.0613	−630.1448	0.0625	0.0916	6.6454	0.1873	−0.1742	7.2173	−0.2606
0.3	0.015	−0.139	−0.0434	−317.8578	−0.0438	0.0571	−742.0800	0.0584	0.1001	6.6528	0.1656	−0.1858	7.2119	−0.2387
0.4	0.070	−0.510	−0.0354	−415.5215	−0.0358	0.0417	−681.7967	0.0426	0.1011	6.6881	0.1400	−0.1795	7.2495	−0.2116
0.5	0.110	−0.774	−0.0160	5.5795	−0.0434	0.0133	5.4701	0.0527	0.0961	6.6975	0.1380	−0.1719	7.2350	−0.2048
0.6	0.131	−0.912	−0.0449	5.8145	−0.0374	0.0573	5.5235	0.0262	0.0962	6.5242	0.1514	−0.1635	7.1431	−0.2200
0.7	0.151	−1.044	−0.0704	6.3052	−0.0434	0.0844	5.8541	0.0170	0.0969	6.5806	0.1743	−0.1661	7.1054	−0.2415
0.8	0.173	−1.191	−0.0746	6.3291	−0.0471	0.0937	5.8399	0.0132	0.0975	6.5639	0.1822	−0.1610	7.0173	−0.2414
0.9	0.192	−1.324	−0.0834	6.2368	−0.0397	0.1114	5.7518	−0.0007	0.0949	6.4505	0.1987	−0.1576	6.9220	−0.2565
1.0	0.209	−1.435	−0.0889	6.2717	−0.0419	0.1249	5.6694	−0.0111	0.1076	6.4254	0.2075	−0.1738	6.8732	−0.2651
1.25	0.252	−1.716	−0.1086	6.5965	−0.0620	0.1374	5.8365	−0.0059	0.1184	6.4642	0.2183	−0.1914	6.9348	−0.2810
1.5	0.284	−1.927	−0.1357	6.7562	−0.0669	0.1521	6.1110	−0.0073	0.1259	6.5839	0.2250	−0.2080	7.0221	−0.2949
2.0	0.319	−2.163	−0.1805	6.9001	−0.0810	0.1916	6.2474	−0.0159	0.1358	6.4724	0.2138	−0.2163	6.9748	−0.2924
2.5	0.328	−2.221	−0.1714	6.9095	−0.0741	0.1830	6.2902	−0.0138	0.1302	6.4547	0.2012	−0.1982	6.9122	−0.2653
3.0	0.323	−2.188	−0.1588	6.9005	−0.0654	0.1760	6.2793	−0.0188	0.1219	6.4096	0.2239	−0.1832	6.7869	−0.2788
4.0	0.324	−2.188	−0.1888	6.9560	−0.0645	0.2000	6.4400	−0.0237	0.1219	6.8339	0.2954	−0.2237	7.2032	−0.3874
5.0	0.307	−2.067	−0.2149	6.9034	−0.0624	0.2301	6.5005	−0.0231	0.1362	7.0221	0.3400	−0.2649	7.3827	−0.4578

Downloaded from http://pubs.geoscienceworld.org/ssa/bssa/article-pdf/112/1/400/5519095/bssa-2021134.1.pdf
by Yefei Ren

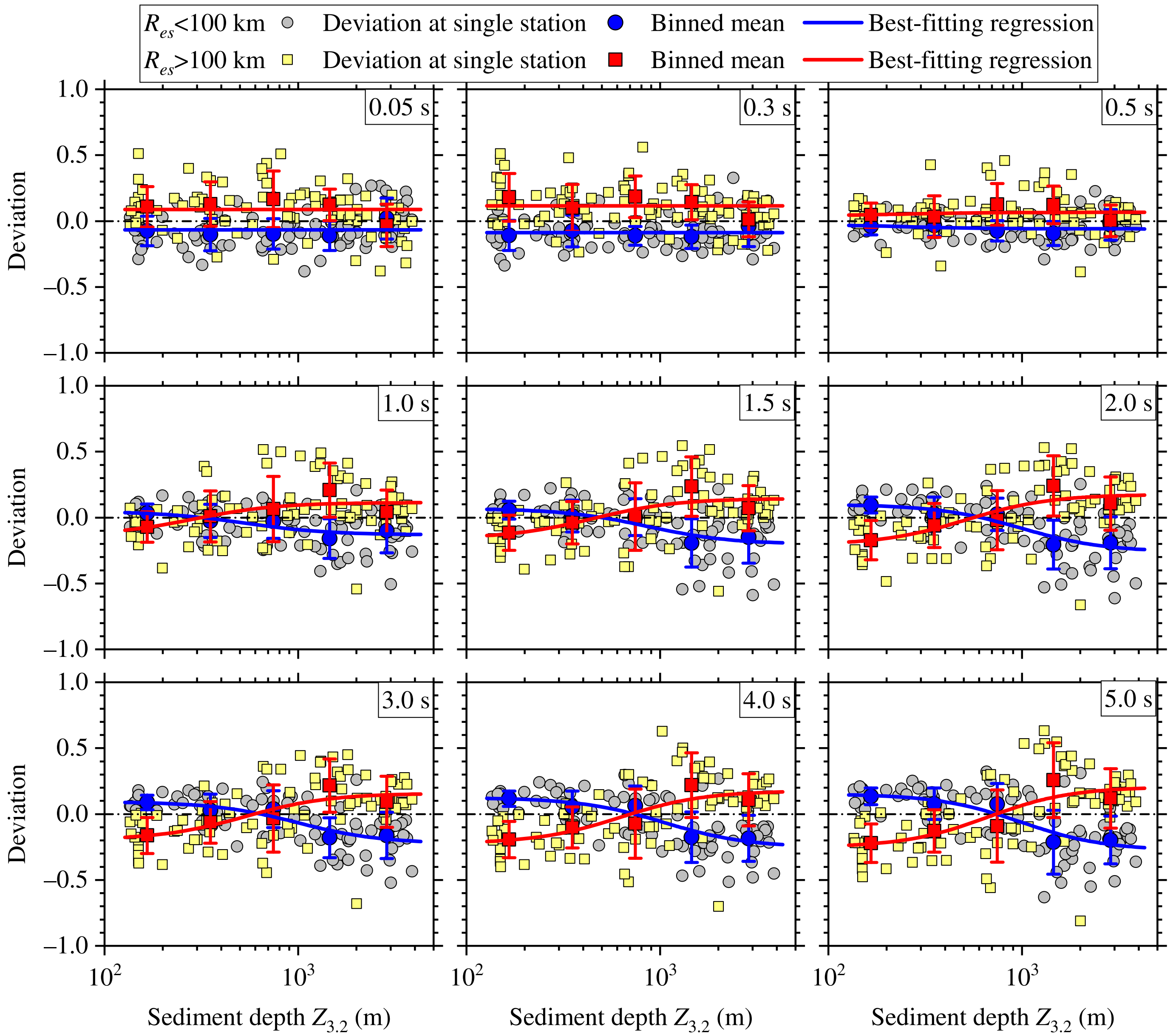

Figure 6. Deviations of additional site amplifications derived from the source-to-site distance-dependent ground-motion sub dataset to those from whole dataset. We consider two sub dataset with distance (R_{es}) less and greater than 100 km, respectively. Solid lines are regressed to describe the distance-dependent deviations as a function of $Z_{3.2}$. The color version of this figure is available only in the electronic edition.

additional site amplifications derived from the distance- and focal depth-dependent dataset are used to calculate deviations to those derived from the corresponding distance-dependent subset. Deviation is denoted by $\ln(A_{\text{dis–dep}}/A_{\text{dis}})$, in which $A_{\text{dis–dep}}$ represents the additional site amplification associated with the distance- and focal depth-dependent dataset.

The pronounced effects of focal depth on additional site amplifications are clearly observed from the deviations plots, as shown in Figure 8. Deviations are generally greater than zero and show an increasing trend with the increasing sedimentary thickness for the shallow crustal earthquakes. However, the negative deviations are observed for the deep subduction earthquakes and show a decreasing trend. Consequently, differences between deviations from shallow crustal and deep subduction earthquakes are much more significant at sites atop the thick sediment. The increasing (or decreasing) trend with sedimentary thickness also shows an obvious dependency on the oscillation period, the sharper trend for the longer oscillation period. Deviation plots indicate that ground motions from shallow crustal earthquakes experience much stronger amplifications than those from the deep subduction earthquakes, especially for long-period ground motions (>1.0 s) at sites atop the thick sediment. Considering that sites atop the thick sediment are mainly located in Kanto basin; this

Downloaded from http://pubs.geoscienceworld.org/ssa/bssa/article-pdf/112/1/400/5519095/bssa-2021134.1.pdf
by Yefei Ren

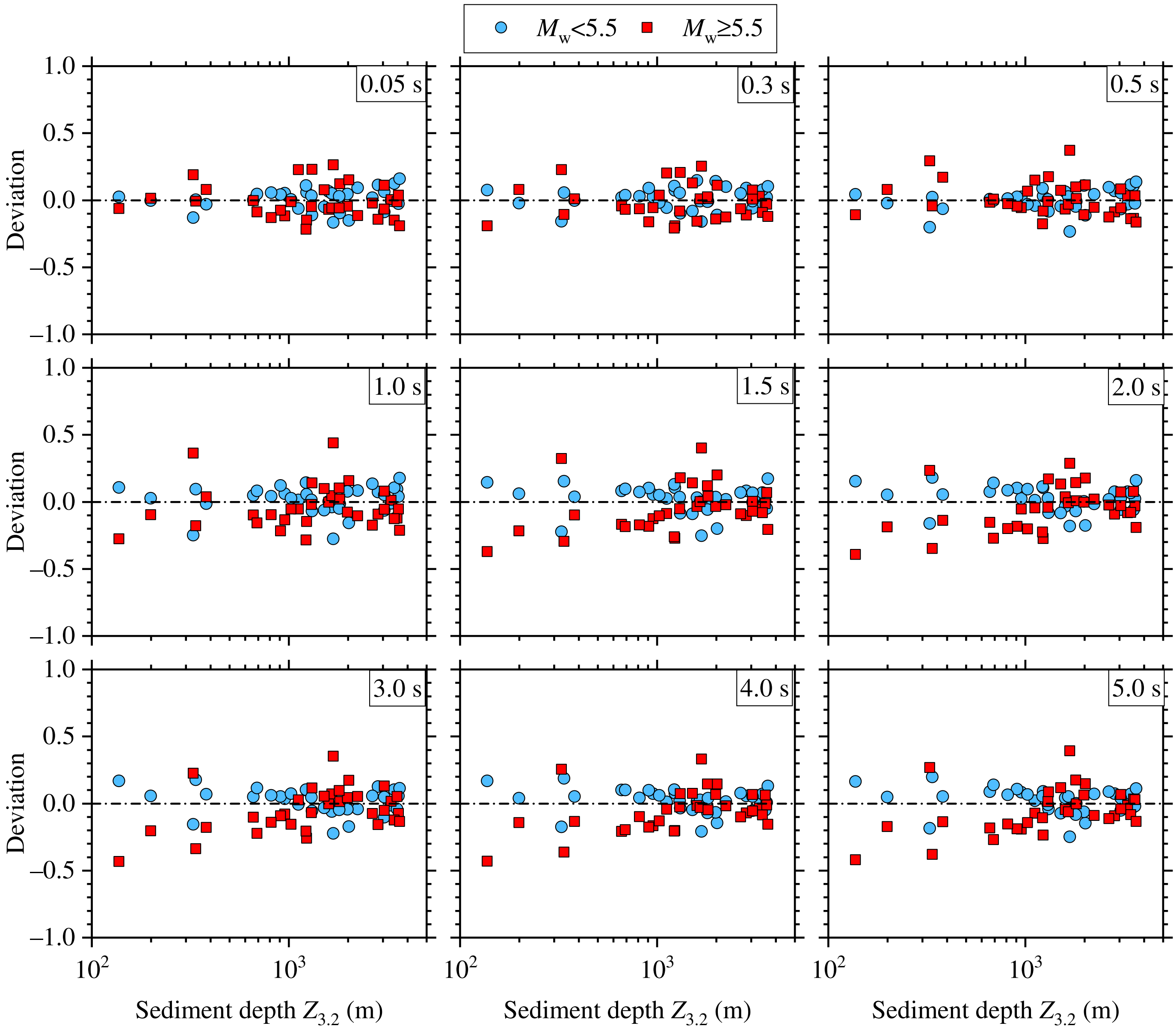

Figure 7. Deviations of additional site amplifications derived from the magnitude (M_w)-dependent local dataset to those from the local dataset. We consider two M_w-dependent local dataset with $M_w < 5.5$ and $M_w \geq 5.5$, respectively. The color version of this figure is available only in the electronic edition.

phenomenon may be ascribed to the shallower incidence angle of the body waves from the shallow crustal earthquakes, which promotes the generation of basin-edge converted surface waves and focusing of energy at basin margins. On the contrary, it is not likely to expect the basin-edge converted surface waves from body waves travelling vertically into the basin from deep subduction earthquakes. Additional site amplifications for 5 s ground shaking at thick sedimentary sites from shallow crustal earthquakes are approximately 3.0 times as great as those from deep subduction earthquakes according to the deviations (about 0.5 and −0.5 from shallow crustal and deep subduction earthquakes, respectively). Focal depth is thus a very key factor affecting the sediment-depth scaling of additional site amplifications. Wirth *et al.* (2019), Lai *et al.* (2020), Miura *et al.* (2019), Thompson *et al.* (2020) have also found that shallow crustal earthquakes appear to produce amplifications in some basins worldwide (Seattle, Tacoma, Los Angeles, and Bogotá basins) that are larger than deep subduction earthquakes. A hyperbolic tangent functional form is also fit to represent the focal depth effects, that is,

$$\ln(A_{\text{dis-dep}}/A_{\text{dis}}) = b_1 \tanh[\ln(Z_{3.2}) - b_2] + b_3, \quad (6)$$

in which b_1, b_2, and b_3 are regression coefficients obtained by nonlinear least-squares regression. Both $R_{es} < 100$ km & Dep < 30 km and $R_{es} > 100$ km & Dep < 30 km subsets are used to fit regressions coefficients for shallow crustal earthquake,

Downloaded from http://pubs.geoscienceworld.org/ssa/bssa/article-pdf/112/1/400/5519095/bssa-2021134.1.pdf
by Yefei Ren

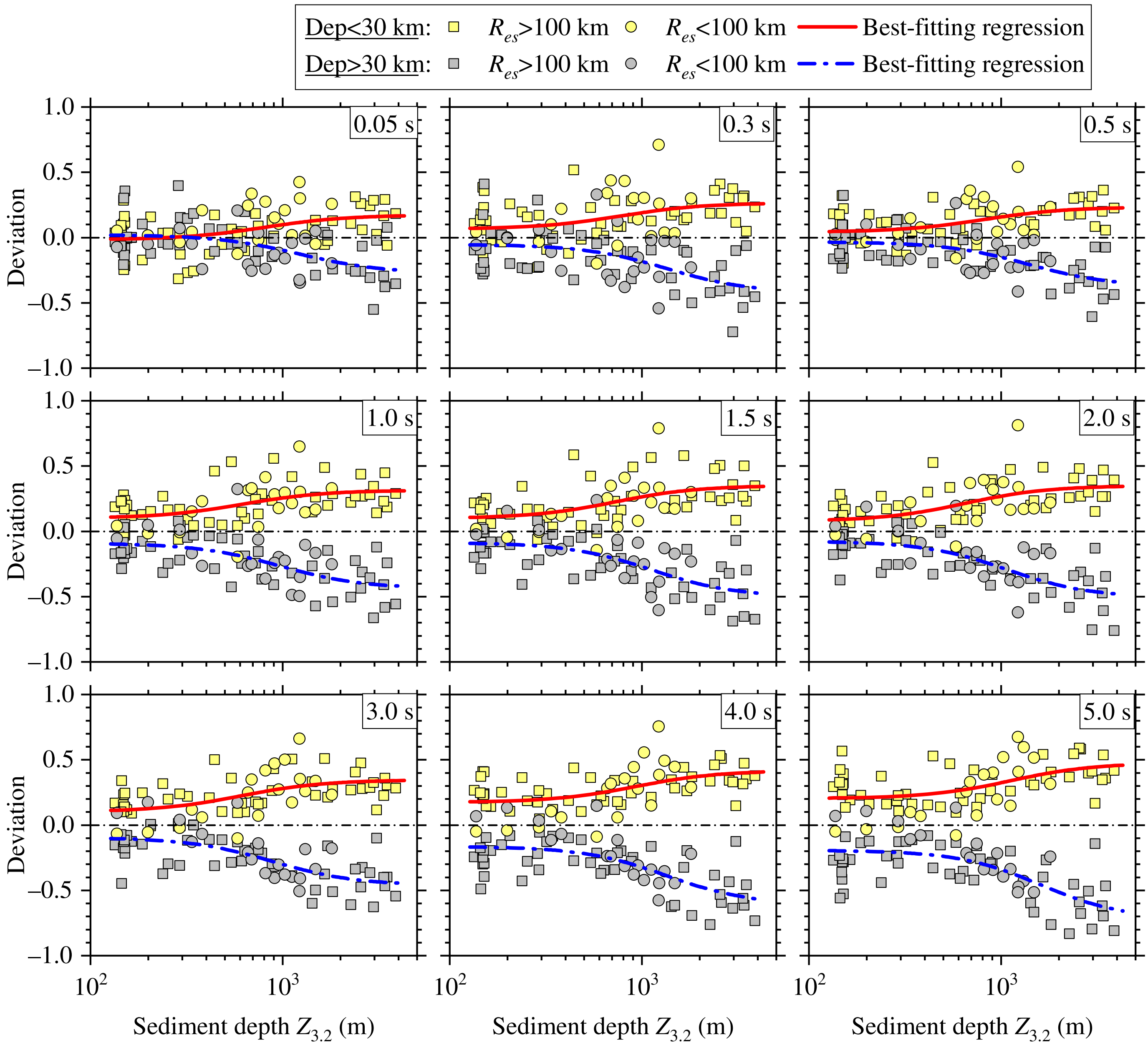

Figure 8. Deviations of additional site amplifications derived from the distance- and focal depth-dependent dataset to those from the corresponding distance-dependent dataset. Four datasets are considered, including distant shallow crustal earthquakes (R_{es} > 100 km & Dep < 30 km), local shallow crustal earthquakes (R_{es} < 100 km & Dep < 30 km), distant deep subduction earthquakes (R_{es} > 100 km & Dep > 30 km), and local deep subduction earthquakes (R_{es} < 100 km & Dep > 30 km). Solid lines are regressed to describe the focal depth-dependent deviations as a function of $Z_{3.2}$. The color version of this figure is available only in the electronic edition.

whereas both R_{es} < 100 km & Dep > 30 km and R_{es} > 100 km & Dep > 30 km subsets are used to fit regressions coefficients for deep subduction earthquake, which are all listed in Table 1. The best-fitting lines well represent the overall variation of focal depth-dependent deviation with sediment depth, as shown in Figure 8.

Source azimuth

Source azimuth (also known as source location relative to site, the direction of propagation, incidence direction, etc.) has also been recognized as a crucial factor in strongly affecting the spatial pattern of amplification in basin (Denolle, Miyake, *et al.*, 2014; Wirth *et al.*, 2019; Moschetti *et al.*, 2020, 2021; Mouzakiotis *et al.*, 2020). It is likely to be due to the irregular basin geometry, which imposes unique effects on the generation and propagation of surface waves in basin. To examine the dependence of additional site amplification on source azimuth, the dataset from distant shallow crustal earthquakes (R_{es} > 100 km & Dep < 30 km) is divided into two

Downloaded from http://pubs.geoscienceworld.org/ssa/bssa/article-pdf/112/1/400/5519095/bssa-2021134.1.pdf
by Yefei Ren

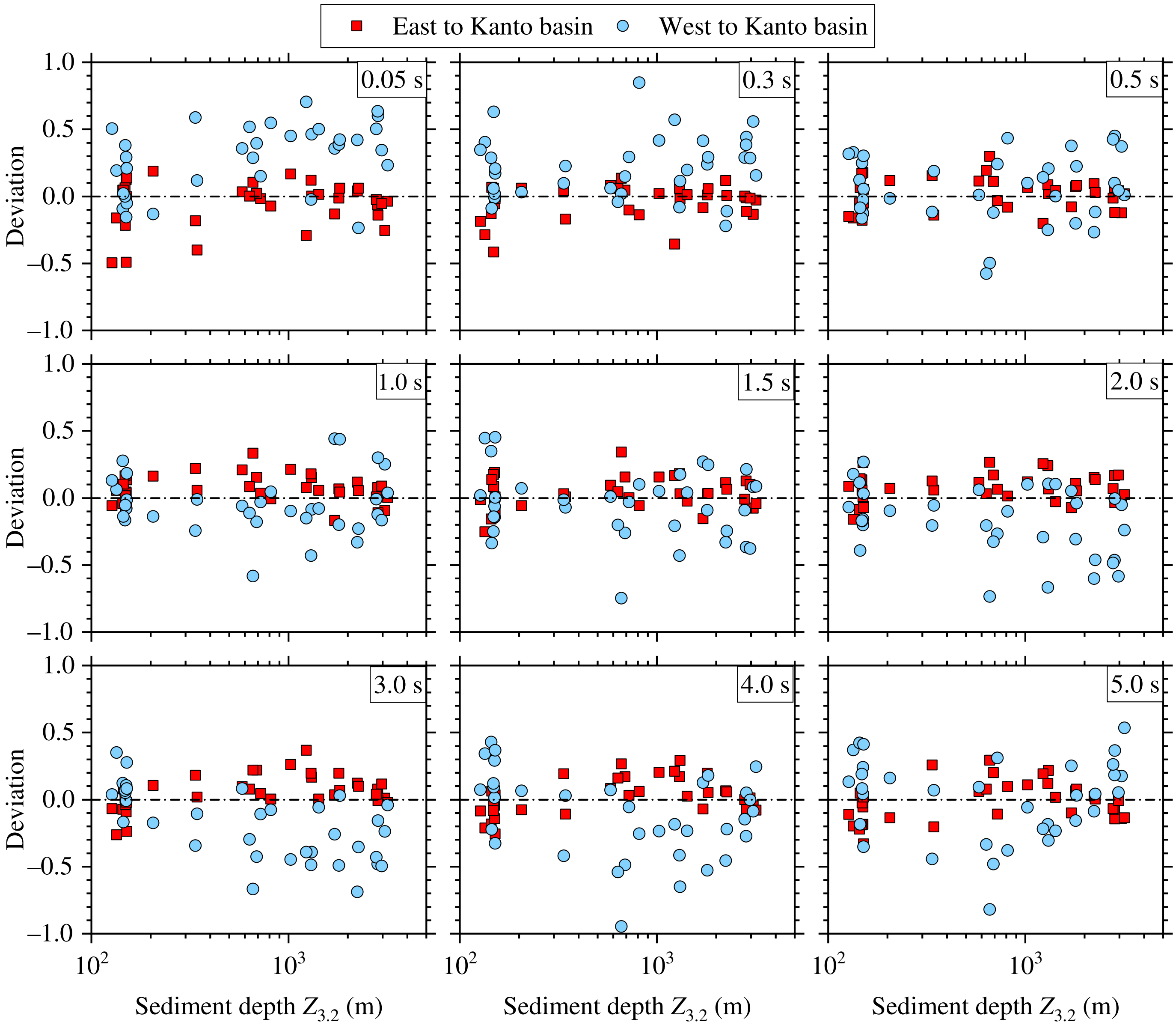

Figure 9. Deviations of additional site amplifications derived from the source azimuth-dependent dataset of distant shallow crustal earthquakes ($R_{es} > 100$ km and Dep < 30 km) to those from the $R_{es} > 100$ km and Dep < 30 km dataset. Two source azimuth-dependent datasets are considered—one with earthquakes east to Kanto basin and the other with earthquakes west to the basin. The color version of this figure is available only in the electronic edition.

groups according to the source azimuths—one with earthquakes east (mainly northeast) to Kanto basin (140.5–142.5° E, 35.5–38.0° N) and the other with earthquakes west (mainly northwest) to Kanto basin (137–140° E, 35.5–38.0° N) (Fig. 2a). Following equation (3), two source azimuth-dependent dataset are used to calculate additional site amplifications, respectively. Because of the sparse number of recordings at a specific station from each source azimuth-dependent dataset (especially the west dataset), the limit on minimum N is relaxed to no less than three. The N values are mainly in the range of 3–5 and 6–18 for datasets with earthquakes west and east to Kanto basin, respectively.

Deviations of additional site amplifications at 35 K-NET stations (mainly in Kanto basin) derived from two source azimuth-dependent dataset to those derived from the $R_{es} > 100$ km & Dep < 30 km dataset are calculated and plotted in Figure 9. Discrepancy of deviations between the east and west dataset indicates that the source azimuth has effects on additional site amplifications. Deviations associated with earthquakes to the east are generally around zero, and they appear to be generally positive at long oscillation periods. However, deviations associated with earthquakes to the west show strong dependence on the oscillation period, from significantly greater than zero to smaller than zero as the oscillation period increases. The small number of recordings used to

Downloaded from http://pubs.geoscienceworld.org/ssa/bssa/article-pdf/112/1/400/5519095/bssa-2021134.1.pdf
by Yefei Ren

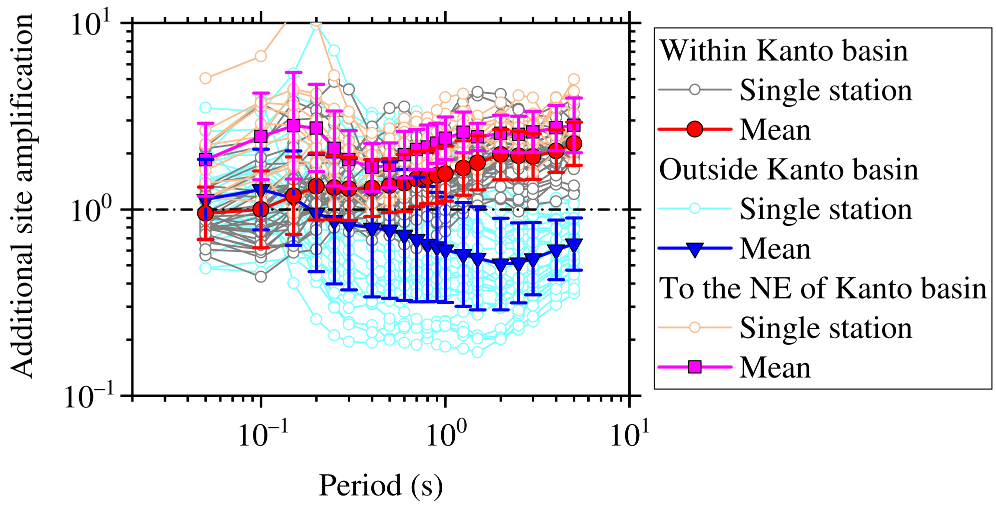

Figure 10. Additional site amplifications with respect to oscillation period calculated for stations at different locations, including within Kanto basin, outside Kanto basin, and in the area northeast (NE) to Kanto basin. Means with one standard deviation (error bar) are plotted for each case. The color version of this figure is available only in the electronic edition.

calculate source azimuth-dependent amplifications may also be responsible for the large scatter in deviations associated with earthquakes to the west. Compared with earthquakes to the east of Kanto basin, long-period ground motions from earthquakes to the west are inclined to experience much smaller amplifications. Surface waves that are induced at the west and northwest boundary of Kanto basin by conversion from incident *S* waves in the west are then attracted by the thick and low-wave-speed sediment in the center of basin (Furumura and Hayakawa, 2007). However, surface waves that are generated at the northeast boundary of Kanto basin by conversion from incident *S* waves in the east propagate into the center of basin and subsequently to the steep west boundary, where the surface waves are reflected back to the center of basin (e.g., Boué *et al.*, 2016). Reflection enhances the surface waves in the basin and may be responsible for the stronger long-period amplification from earthquakes to the east.

ADDITIONAL SITE AMPLIFICATIONS WITHIN AND OUTSIDE KANTO BASIN

According to the aforementioned analyses, long-period ground motions at sites atop the thick sediment from distant shallow crustal earthquakes experience much stronger amplifications than from local deep subduction earthquakes. This is likely because the shallower incidence angle in the distant shallow crustal earthquakes promotes the generation of surface waves at basin edges. Hereinafter, we mainly pay close attention to the additional site amplifications at 127 K-NET stations (shown in Figs. 1 and 2a, and listed in Table S1, available in supplemental material to this article) derived from the R_{es} > 100 km & Dep < 30 km dataset. In these stations, 34 stations are within the Kanto basin, given that the contour line of $Z_{3.2}$ equal to 1500 m is defined as the boundary of Kanto basin in this study. Some stations within and around other small-size basins (e.g., Sendai plain, Yamagata basin, and Mitsuka basin) to the north of Kanto basin are not analyzed in detail in this study. The sedimentary thicknesses in these small-size basins are much shallower than those in Kanto basin.

Additional site amplifications at 34 stations within Kanto basin are compared with those at 29 stations with shallow sedimentary thickness (in general $Z_{3.2}$ < 500 m) mainly to the west of the Kanto basin, as shown in Figure 10. Mean additional site amplifications within Kanto basin are generally equal to 1.0 for short-period ground motions (≤0.1 s), and then gradually increase as the oscillation period increases and reaches a maximum of approximately 2.25 for long-period ground motions at 5.0 s. The overall trend of amplification with oscillation period in our study is very similar to those proposed by Marafi *et al.* (2017) for the Yufutsu and Konsen basins during the *M* 8.3 Tokachi–Oki earthquake and the Niigata basin during the *M* 9.0 Tohoku earthquake, while significantly different from the strange trend proposed by Marafi *et al.* (2017) for Kanto basin during the *M* 9.0 Tohoku earthquake over 200 km to the northeast of Kanto basin. They found that amplifications in Kanto basin exceed one at oscillation periods less than 1.4 and larger than 3.0 s, and the maximum amplification (~2–3) occurs at short periods (<0.3 s). The specific earthquake (*M* 9.0 Tohoku earthquake) considered may be responsible for the strange trend of amplification in Kanto basin by Marafi *et al.* (2017). On the contrary, mean amplifications calculated for stations outside the Kanto basin are generally smaller than 1.0, except for the short-period ground motions (≤0.1 s). They show an approximately decreasing trend from ~1.2 to ~0.5, as the oscillation period increases from 0.05 to 2.0 s, and then very slowly escalate to ~0.65 at period of 5.0 s with the increasing oscillation period. Mean amplifications within Kanto basin are about 3.5 times larger than those outside the basin for oscillation periods ranging from 2.0 to 5.0 s. The pronounced discrepancy of amplification estimates between stations within and outside Kanto basin indicates that long-period ground motions is subject to be strongly amplified by Kanto basin. Such strong amplifications on long-period ground motions

Downloaded from http://pubs.geoscienceworld.org/ssa/bssa/article-pdf/112/1/400/5519095/bssa-2021134.1.pdf
by Yefei Ren

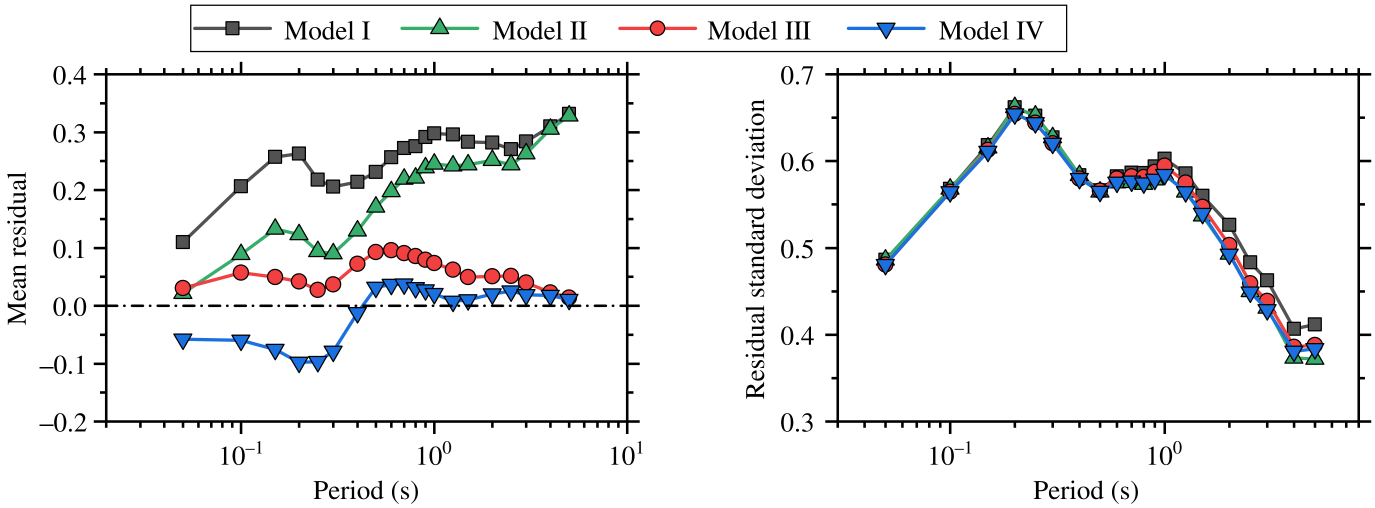

Figure 11. Means and standard deviations for residuals over all stations considered. Residuals at 127 K-NET stations between the amplifications derived from the dataset with distant shallow crustal earthquakes and the predicted amplifications by four models with different complexity are calculated. Model I: just considering the sediment-depth scaling, model II: considering the effects of source-to-site distance on sediment-depth scaling, model III: considering the effects of focal depth on sediment-depth scaling, and model IV: considering both effects of distance and focal depth on sediment-depth scaling. The color version of this figure is available only in the electronic edition.

within Kanto basin are very important for the reliable assessment of its seismic hazard.

We further note that mean amplifications calculated for stations northeast (NE) to Kanto basin with $Z_{3.2}$ equal to 650–1500 m are significantly higher than those within Kanto basin. Mean amplifications for these stations NE to Kanto basin are approximately in the range of 2–3 for the short-period ground motions (0.05–0.3 s). They also gradually increase as the oscillation period increases from 0.4 to 5.0 s, up to a maximum of approximately 3.0 at 5.0 s. Similarly, much stronger basin amplifications occurred in the area NE to Kanto basin, according to the amplification maps provided by Denolle, Miyake, *et al.* (2014). Different from the west boundary, sedimentary thickness in the area NE to Kanto basin slowly decreases from the NE boundary of Kanto basin to NE far from the Kanto basin (Fig. 1). $Z_{3.2}$ values in a large area NE to Kanto basin are in the range of 500–1500 m. Moreover, there are large Z_1 values, about 450–1000 m also in this area (Table S1). We thus infer that the Kanto basin defined in this study can be further extended to the NE. The basin edge effects may be mainly responsible for the pronounced basin amplifications occurred in the area NE to Kanto basin.

Integrating multiple factors, including basin depth, source-to-site distance, and focal depth, additional site amplifications can be empirically expressed as

$$\ln(A_s) = c_0 \ln(Z_{3.2}) + c_1 + a_1 \tanh[\ln(Z_{3.2}) - a_2] + a_3 + b_1 \tanh[\ln(Z_{3.2}) - b_2] + b_3. \quad (7)$$

Coefficients are all listed in Table 1. c_0 and c_1 indicate sediment depth-dependent effects; a_1, a_2, and a_3 indicate distance-dependent effects; and b_1, b_2, and b_3 indicate focal depth-dependent effects. In Kanto basin, the additional site amplification expressed by the empirical model in equation (7) can be attributed to the basin effects, which is not completely covered by the site class term in Zhao06 model. Combining the site class term in Zhao06 GMPE, additional site amplifications predicted by equation (7) can be used to represent the whole site effects on ground motions in Kanto basin, including the basin amplifications.

To evaluate the model performance with its complexity increased, we calculate the residuals at 127 K-NET stations between the calculated amplifications using the dataset from distant shallow crustal earthquakes and the predicted amplifications by four models with different complexity, that is, model I just considering the sediment-depth scaling, model II considering the effects of source-to-site distance on sediment-depth scaling, model III considering the effects of focal depth on sediment-depth scaling, and model IV considering both effects of source-to-site distance and focal depth on sediment-depth scaling. The means and standard deviations for residuals over all 127 stations considered are plotted in Figure 11 in the cases of four models used, respectively. As the increasing of model complexity, there is no obvious change in the residual standard deviations, whereas significant changes occur in residual means. Model complexity can promote the residual means to shift toward zero, indicating the better performance as the model complexity increased. Either distance or focal depth is capable of improving the model performance, but focal depth works much better. The model considering both effects of distance and focal depth on sediment-depth scaling shows the best performance with residual means very close to zero,

Downloaded from http://pubs.geoscienceworld.org/ssa/bssa/article-pdf/112/1/400/5519095/bssa-2021134.1.pdf
by Yefei Ren

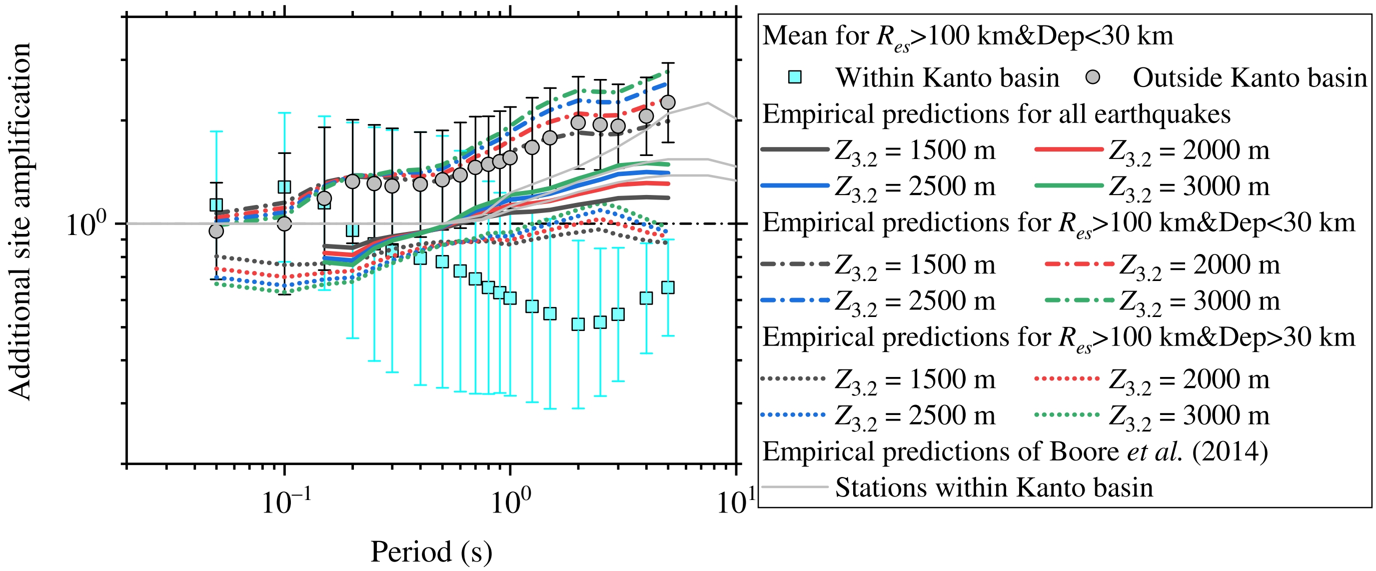

Figure 12. Additional site amplification predictions based on the empirical models from our study and Boore *et al.* (2014). The color version of this figure is available only in the electronic edition.

especially at periods longer than 0.3 s. To improve the prediction reliability, it is better to consider the effects of source-to-site distance and focal depth.

$Z_{3.2}$ values for stations within Kanto basin are mainly in the range of 1500–3000 m. Setting $Z_{3.2}$ values to 1500, 2000, 2500, and 3000 m, respectively, we provide the additional site amplification predictions for Kanto basin based on the empirical model (equation 7) developed in this study, as shown in Figure 12. Here, we take three cases into consideration, including all earthquakes with source-to-site distance and focal depth out of consideration, distant shallow crustal earthquakes (R_{es} > 100 km & Dep < 30 km), and distant deep subduction earthquakes (R_{es} > 100 km & Dep > 30 km). Meanwhile, the basin amplification predictions derived from the empirical model proposed by Boore *et al.* (2014) are plotted and compared in Figure 11. They developed the empirical model of basin amplification as a function of δZ_1, which is represented as Z_1 minus the prediction of an empirical model relating Z_1 to V_{S30}. According to their empirical model, we calculate the basin amplification predictions for stations within Kanto basin of which Z_1 and V_{S30} values are listed in Table S1.

With the source-to-site distance and focal depth out of consideration, the additional site amplification predictions are up to approximately 1.5 at long periods (2–5 s). They are significantly smaller than those at long periods (approximately 2.0–3.0) derived from distant shallow crustal earthquakes, whereas slightly greater than those (~1.0 or more) from distant deep subduction earthquakes. The empirical predictions from our study well describe the enhanced basin amplifications within Kanto basin during distant shallow crustal earthquakes. Basin amplifications at long periods predicted by the empirical model of Boore *et al.* (2014) for stations within Kanto basin are mainly in the range of 1.3–2.0. Our predictions with distance and focal depth out of consideration are in good agreement with their predictions at some station and also smaller than their predictions at other stations. However, predictions from Boore *et al.* (2014) are generally smaller than those predicted for distant shallow crustal earthquakes by our model.

CONCLUSIONS

Basin effects are very fundamental for seismic hazard assessment, because most metropolitan areas are located in sedimentary basins worldwide. Ground-motion residuals with respect to the GMPE developed by Zhao *et al.* (2006) for Japan are calculated and decomposed to evaluate additional site amplifications at over 200 K-NET stations within and around Kanto basin. Additional site amplifications in Kanto basin can be attributed to the basin amplification effects, which are not completely included in the site class term in Zhao06 model. In addition to the effects of sediment depth, we pay special attention to the potential effects of multiple source-dependent factors on additional site amplifications, including source-to-site distance, magnitude, focal depth, and source azimuth. We find that amplifications for long-period ground motions gradually enlarge with the sediment depth $Z_{3.2}$ increased. Magnitude has negligible effects on the amplifications. However, source-to-site distance, focal depth, and source azimuth all exert nonnegligible effects on the amplifications, especially the focal depth.

Thick sedimentary sites appear to amplify the long-period ground motions from distant earthquakes much more greatly than from local earthquakes. Meanwhile, ground motions from shallow crustal earthquakes generally have much stronger amplifications than those from deep subduction earthquakes. Effects of focal depth on amplifications show significant dependency on the oscillation period and sedimentary thickness. Focal

Downloaded from http://pubs.geoscienceworld.org/ssa/bssa/article-pdf/112/1/400/5519095/bssa-2021134.1.pdf
by Yefei Ren

depth is capable of causing much more notable effects on amplifications for long-period ground motions (>1.0 s) at sites with deep sedimentary thickness. We also note that weaker amplifications are, in general, inclined to occur in long-period ground motions during earthquakes west to Kanto basin than those during earthquakes east to the basin. Moreover, an empirical model integrating sediment depth and source-dependent factors (source-to-site distance and focal depth) is developed to predict the amplification effects. Our model well describes the source-dependent amplifications. This empirical model is the first one to predict basin amplifications in Kanto basin, considering the source-dependent factors.

Finally, we focus on the addition site amplifications in the worst case of distant shallow crustal earthquakes. Additional site amplifications within Kanto basin show an increasing trend with respect to the oscillation period. However, the estimated amplifications for stations with shallow sedimentary thickness outside Kanto basin are generally characterized by the decreasing trend with the increasing oscillation period. The mean amplification within Kanto basin is up to about 2.25 at period of 5.0 s, whereas 0.65 outside Kanto basin. It thus can be inferred that long-period ground-motion predictions, underestimated within basin whereas overestimated outside basin, are provided by GMPEs with the basin effects out of consideration. We also note that the largest amplifications occur at stations located northeast to Kanto basin, rather than those within the basin. Their mean amplifications are larger than 2.0 at periods of 0.1–0.3 s and ≥1.0 s, and reach about 3.0 at periods of 0.15 and 5.0 s. We inferred that their stronger amplification may result from the basin edge effects at the northeast edge of Kanto basin.

DATA AND RESOURCES

Ground-motion data from the K-NET strong-motion seismography networks were downloaded at www.kyoshin.bosai.go.jp. The high-resolution focal locations were obtained from the Japan Meteorological Agency (JMA) Uniformed Hypocenter Catalog at https://hinetwww11.bosai.go.jp/auth/JMA/jmalist.php?LANG=en. The Global Centroid Moment Tensor (Global CMT) Project database was searched using https://www.globalcmt.org/CMTsearch.html. The Focal Mechanism Catalog from the High Sensitivity Seismography Network Japan (Hi-net) was searched using https://www.hinet.bosai.go.jp/AQUA/aqua_catalogue.php?LANG=en. The subsurface velocity structure model was derived from the official website (https://www.jishin.go.jp/evaluation/seismic_hazard_map/lpshm/12_choshuki_dat/) of the Headquarters for Earthquake Research Promotion (HERP). All websites were last accessed in February 2020. The supplemental material includes Table S1 describing the information on 127 K-NET stations where additional site amplifications are derived from recordings during the distant shallow crustal earthquakes.

DECLARATION OF COMPETING INTERESTS

The authors acknowledge that there are no conflicts of interest recorded.

ACKNOWLEDGMENTS

The authors are very grateful to Associate Editor Hiroshi Kawase, Grace Parker, and an anonymous reviewer for their valuable comments that improved this article. This work is supported by the National Key R&D Program of China (Grant Number 2019YFE0115700), Natural Science Foundation of Heilongjiang Province (Grant Number LH2020E021), and National Natural Science Foundation of China (Grant Number 51808514).

REFERENCES

Abraham, J. R., C. G. Lai, and A. Papageorgiou (2015). Basin-effects observed during the 2012 Emilia earthquake sequence in northern Italy, *Soil Dynam. Earthq. Eng.* **78,** 230–242.

Abrahamson, N., N. Gregor, and K. Addo (2016). BC Hydro ground motion prediction equations for subduction earthquakes, *Earthq. Spectra* **32,** 23–44.

Abrahamson, N. G., and R. R. Youngs (1992). A stable algorithm for regression analyses using the random effects models, *Bull. Seismol. Soc. Am.* **82,** 505–510.

Ancheta, T. D., R. B. Darragh, J. P. Stewart, E. Seyhan, W. J. Silva, B. S.-J. Chiou, K. E. Wooddell, R. W. Graves, A. R. Kottke, D. M. Boore, *et al.* (2013). PEER NGA-West2 database, *PEER Rept., 2013/03*, 122 pp, available at https://peer.berkeley.edu/peer-reports (last accessed October 2019).

Bard, P.-Y., and M. Bouchon (1980). The seismic response of sediment-filled valleys. Part I. the case of incident SH waves, *Bull. Seismol. Soc. Am.* **70,** 1263–1286.

Boore, D. M. (2005). On pads and filters: Processing strong-motion data, *Bull. Seismol. Soc. Am.* **95,** 745–750.

Boore, D. M., J. P. Stewart, E. Seyhan, and G. M. Atkinson (2013). NGA-West2 equations for predicting response spectral accelerations for shallow crustal earthquakes, *PEER Rept. 2013/05*, 10 pp., available at https://peer.berkeley.edu/peer-reports (last accessed January 2017).

Boore, D. M., J. P. Stewart, E. Seyhan, and G. M. Atkinson (2014). NGA-West2 equations for predicting PGA, PGV, and 5% damped PSA for shallow crustal earthquakes, *Earthq. Spectra* **30,** 1057–1085.

Borcherdt, R. D. (1970). Effects of local geology on ground motion near San Francisco bay, *Bull. Seismol. Soc. Am.* **60,** 29–61.

Boué, P., M. Denolle, N. Hirata, S. Nakagawa, and G. C. Beroza (2016). Beyond basin resonance: Characterizing wave propagation using a dense array and the ambient seismic field, *Geophys. J. Int.* **206,** 1261–1272.

Choi, Y., J. P. Stewart, and R. W. Graves (2005). Empirical model for basin effects accounts for basin depth and source location, *Bull. Seismol. Soc. Am.* **95,** 1412–1427.

Cornou, C., and P.-Y. Bard (2003). Site-to-bedrock over 1D transfer function ratio: An indicator of the propagation of edge-generated surface waves, *Geophys. Res. Lett.* **30,** 1453–1458.

Cornou, C., P.-Y. Bard, and M. Dietrich (2003). Contribution of dense array analysis to the identification and quantification of basin-edge-induced waves, part II: Application to Grenoble basin (French Alps), *Bull. Seismol. Soc. Am.* **93,** 2624–2648.

Dhakal, Y. P., and H. Yamanaka (2013). An evaluation of 3-D velocity models of the Kanto basin for long-period ground motion simulations, *J. Seismol.* **17,** 1073–1102.

Downloaded from http://pubs.geoscienceworld.org/ssa/bssa/article-pdf/112/1/400/5519095/bssa-2021134.1.pdf
by Yefei Ren

Dhakal, Y. P., W. Suzuki, T. Kunugi, and S. Aoi (2015). Ground motion prediction equations for absolute velocity response spectra (1-10 s) in Japan for earthquake early warning, *J. Jpn. Assoc. Earthq. Eng.* **15,** 91–111.

Denolle, M. A., E. M. Dunham, G. A. Prieto, and G. C. Beroza (2014). Strong ground motion prediction using virtual earthquakes, *Science* **343,** 399–403.

Denolle, M. A., H. Miyake, S. Nakagawa, N. Hirata, and G. C. Beroza (2014). Long-period seismic amplification in the Kanto basin from the ambient seismic field, *Geophys. Res. Lett.* **41,** 2319–2325.

Furumura, T., and T. Hayakawa (2007). Anomalous propagation of long-period ground motions recorded in Tokoy during the 23 October 2004 Mw6.6 Niigata-Ken Chuetsu, Japan, earthquake, *Bull. Seismol. Soc. Am.* **97,** 863–880.

Graves, R. W., A. Pitarka, and P. G. Somerville (1998). Ground-motion amplification in the Santa Monica area: Effects of shallow basin-edge structure, *Bull. Seismol. Soc. Am.* **88,** 1224–1242.

Hartzell, S., A. L. Leeds, L. Ramirez-Guzman, J. P. Allen, and R. G. Schmitt (2016). Seismic site characterization of an urban sedimentary basin, Livermore valley, California: Site response, basin-edge-induced surface waves, and 3D simulations, *Bull. Seismol. Soc. Am.* **106,** 609–631.

Hashima, A., T. Sato, H. Sato, K. Asao, H. Furuya, S. Yamamoto, K. Kameo, T. Miyauchi, T. Ito, N. Tsumura, *et al.* (2016). Simulation of tectonic evolution of the Kanto basin of Japan since 1 Ma due to subduction of the Pacific and Philippine Sea plates and the collision of the Izu-Bonin arc, *Tectonophysics* **679,** 1–14.

Hayes, G. P., D. J. Wald, and R. L. Johnson (2012). Slab1.0: A three-dimensional model of global subduction zone geometrics, *J. Geophys. Res.* **117,** no. B01302, doi: 10.1029/2011JB008524.

Irikura, K., and H. Miyake (2011). Recipe for predicting strong ground motion from crustal earthquake scenarios, *Pure Appl. Geophys.* **168,** 85–104.

Ishise, M., H. Miyake, and K. Koketsu (2015). Dual subduction tectonics and plate dynamics of central Japan shown by three-dimensional P-wave anisotropic structure, *Phys. Earth Planet. In.* **244,** 49–68.

Iwata, T., and K. Asano (2011). Characterization of the heterogeneous source model of intraslab earthquakes toward strong ground motion prediction, *Pure Appl. Geophys.* **168,** 117–124.

Kawase, H. (1996). The case of the damage belt in Kobe: "The basin-edge effect," constructive interference of the direct S-wave with the basin-induced diffracted/Rayleigh waves, *Seismol. Res. Lett.* **67,** 25–34.

Kawase, H., and K. Aki (1989). A study on the response of a soft basin for incident S, P, and Rayleigh waves with special reference to the long duration observation in Mexico city, *Bull. Seismol. Soc. Am.* **79,** 1361–1382.

Kawase, H., and T. Sato (1992). Simulation analysis of strong motions in the Ashigara valley considering one- and two-dimensional geological structures, *J. Phys. Earth* **40,** 27–56.

Koketsu, K., and M. Kikuchi (2000). Propagation of seismic ground motion in the Kanto basin, Japan, *Science* **288,** 1237–1239.

Koketsu, K., H. Miyake, Afnimar, and Y. Tanaka (2009). A proposal for a standard procedure of modeling 3-D velocity structures and its application to the Tokyo metropolitan area, Japan, *Tectonophysics* **472,** 290–300.

Lai, V. H., R. W. Graves, C. Yu, Z. Zhan, and D. V. Helmberger (2020). Shallow basin structure and attenuation are key to predicting long shaking duration in Los Angeles basin, *J. Geophys. Res.* **125,** e2020JB019663 , doi: 10.1029/2020JB019663.

Luzi, L., M. D'Amico, M. Massa, and R. Puglia (2019). Site effects observed in the Norcia intramountain basin (central Italy) exploiting a 20-year monitoring, *Bull. Earthq. Eng.* **17,** 97–118.

Mai, P. M., P. Spudich, and J. Boatwright (2005). Hypocenter locations in finite-source rupture models, *Bull. Seismol. Soc. Am.* **95,** 965–980.

Marafi, N. A., M. O. Eberhard, J. W. Berman, E. A. Wirth, and A. D. Frankel (2017). Effects of deep basin on structural collapse during large subduction earthquakes, *Earthq. Spectra* **33,** 963–997.

Miura, H., T. Okamura, M. Matsuoka, M. Leal, H. Garcia, and N. Pulido (2019). Empirical models for surface- and body-wave amplifications of response spectra in the Bogota basin, Colombia, *Bull. Seismol. Soc. Am.* **109,** 987–1004.

Miyake, H., and K. Koketsu (2005). Long-period ground motions from a large offshore earthquake: The case of the 2004 off the Kii peninsula earthquake, Japan, *Earth Planets Space* **57,** 203–207.

Morikawa, N., and H. Fujiwara (2013). A new ground motion prediction equation for Japan applicable up to M9 mega-earthquake, *J. Disast. Res.* **8,** 878–888.

Moschetti, M. P., D. Churchwell, E. M. Thompson, J. M. Rekoske, E. Wolin, and O. S. Boyd (2021). Seismic wave propagation and basin amplification in the Wasatch Front, Utah, *Seismol. Res. Lett.* doi: 10.1785/0220200449.

Moschetti, M. P., E. M. Thompson, J. Rekoske, M. G. Hearne, P. M. Powers, D. E. McNamara, and C. Tape (2020). Ground-motion amplification in Cook Inlet region, Alaska, from intermediate-depth earthquakes, including the 2018 Mw 7.1 Anchorage earthquake, *Seismol. Res. Lett.* **91,** 142–152.

Mouzakiotis, E., V. Karastathis, N. Voulgaris, and P. Papadimitriou (2020). Site amplification assessment in the east Corinth Gulf using 3D finite-difference modeling and local geophysical data, *Pure Appl. Geophys.* **177,** 3871–3889.

Murotani, S., S. Matsushima, T. Azuma, K. Irikura, and S. Kitagawa (2015). Scaling relations of source parameters of earthquakes occurring on inland crustal mega-fault systems, *Pure Appl. Geophys.* **172,** 1371–1381.

Murotani, S., H. Miyake, and K. Koketsu (2008). Scaling of characterized slip models for plate-boundary earthquakes, *Earth Planets Space* **60,** 987–991.

Olsen, K. B. (2000). Site amplification in the Los Angeles basin from three-dimensional modeling of ground motion, *Bull. Seismol. Soc. Am.* **90,** S77–S94.

Pacor, F., D. Bindi, L. Luzi, S. Parolai, S. Marzorati, and G. Monachesi (2007). Characteristics of strong ground motion data recorded in the Gubbio sedimentary basin (central Italy), *Bull. Earthq. Eng.* **5,** 27–43.

Roten, D., D. Fah, K. B. Olsen, and D. Giardini (2008). A comparison of observed and simulated site response in the Rhone valley, *Geophys. J. Int.* **173,** 958–978.

Rovelli, A., L. Scognamiglio, F. F. Marra, and A. Caserta (2001). Edge-diffracted 1-sec surface waves observed in a small-size intramountain basin (Colfiorito, central Italy), *Bull. Seismol. Soc. Am.* **91,** 1851–1866.

Downloaded from http://pubs.geoscienceworld.org/ssa/bssa/article-pdf/112/1/400/5519095/bssa-2021134.1.pdf
by Yefei Ren

Sato, T., R. W. Graves, and P. G. Somerville (1999). Three-dimensional finite-difference simulations of long-period strong motions in the Tokyo metropolitan area during the 1990 Odawara earthquake (MJ 5.1) and the Great 1923 Tokyo earthquake (Ms 8.2) in Japan, *Bull. Seismol. Soc. Am.* **89,** 579–607.

Semblat, J. F., A. M. Duval, and P. Dangla (2002). Seismic site effects in a deep alluvial basin: Numerical analysis by the boundary element method, *Comput. Geotech.* **29,** 573–585.

Skarlatoudis, A., M. Hosseini, and P. Somerville (2015). Basin amplification factors for Cascadia from the 2011 Tohoku earthquake, *Research Rept., U.S. Geol. Surv. (USGS)*, 14–36, available at https://earthquake.usgs.gov/cfusion/external_grants/reports/G14AP00009.pdf (last accessed March 2018).

Smerzini, C., R. Paolucci, and M. Stupazzni (2011). Comparison of 3D, 2D, and 1D numerical approaches to predict long period earthquake ground motion in the Gubbio plain, central Italy, *Bull. Earthq. Eng.* **9,** 2007–2029.

Stein, R. S., S. Toda, T. Parsons, and E. Grunewald (2006). A new probabilistic seismic hazard assessment for greater Tokyo, *Phil. Trans. Math. Phys. Eng. Sci.* **364,** 1965–1988.

Thompson, M., E. A. Wirth, A. D. Frankel, J. R. Hartog, and J. E. Vidale (2020). Basin amplification effects in the Puget Lowland, Washington, from strong-motion recordings and 3D simulations, *Bull. Seismol. Soc. Am.* **110,** 534–555.

Tsuno, S., H. Yamanaka, S. Midorikawa, S. Yamamoto, H. Miura, S. Sakai, N. Hirata, K. Kasahara, H. Kimura, and T. Aketagawa (2012). Characteristics of long-period ground motions in the Tokyo metropolitan area and its vicinity, by recording data of the 2011 off the Pacific coast of Tohoku earthquake (Mw9.0) and the aftershocks, *J. Jpn. Assoc. Earthq. Eng.* **12,** 102–116 (in Japanese with English abstract).

Volk, O., S. Shani-Kadmiel, Z. Gvirtzman, and M. Tsesarsky (2017). 3D effects of sedimentary wedges and subsurface canyons: Ground-motion amplification in the Israeli coastal plain, *Bull. Seismol. Soc. Am.* **107,** 1324–1335.

Wang, G.-Q., G.-Q. Tang, D. M. Boore, G. V. N. Burbach, C. R. Jackson, X.-Y. Zhou, and Q.-L. Lin (2006). Surface waves I the Western Taiwan coastal plain from an aftershock of the 1999 Chi-Chi, Taiwan, earthquake, *Bull. Seismol. Soc. Am.* **96,** 821–845.

Wang, H.-Y., and S.-Y. Wang (2015). A new method for estimating Vs30 from a shallow shear-wave velocity profile (depth < 30 m), *Bull. Seismol. Soc. Am.* **105,** 1359–1370.

Wen, R., P. Xu, H. Wang, and Y. Ren (2018). Single-station standard deviation using strong-motion data from Sichuan region, China, *Bull. Seismol. Soc. Am.* **108,** 2237–2247.

Wirth, E. A., J. E. Vidale, A. D. Frankel, T. L. Pratt, N. A. Marafi, M. Thompson, and W. J. Stephenson (2019). Source-dependent amplification of earthquake ground motions in deep sedimentary basins, *Geophys. Res. Lett.* **46,** 6443–6450.

Wu, F., D. Okaya, H. Sato, and N. Hirata (2007). Interaction between two subducting plates under Tokyo and its possible effects on seismic hazards, *Geophys. Res. Lett.* **34,** L18301 , doi: 10.1029/2007GL030763.

Zhao, J. X., J. Zhang, A. Asano, Y. Ohno, T. Oouchi, T. Takahashi, H. Ogawa, K. Irikura, H. K. Thio, P. G. Somerville, *et al.* (2006). Attenuation relations of strong ground motion in Japan using site classification based on predominant period, *Bull. Seismol. Soc. Am.* **96,** 898–913.

Zhao, J. X., S. Zhou, P. Gao, T. Long, Y. Zhang, H. K. Thio, M. Lu, and D. A. Rhoades (2015). An earthquake classification scheme adapted for Japan determined by the goodness of fit for ground-motion

prediction equations, *Bull. Seismol. Soc. Am.* **105,** 2750–2763.

Zhao, J. X., S. Zhou, J. Zhou, C. Zhao, H. Zhang, Y. Zhang, P. Gao, X. Lan, D. Rhoades, Y. Fukushima, *et al.* (2016). Ground-motion prediction equations for shallow crustal and upper-mantle earthquakes in Japan using site class and simple geometric attenuation functions, *Bull. Seismol. Soc. Am.* **106,** 1552–1569.

Manuscript received 10 May 2021
Published online 12 October 2021

Downloaded from http://pubs.geoscienceworld.org/ssa/bssa/article-pdf/112/1/400/5519095/bssa-2021134.1.pdf
by Yefei Ren